The Astrophysical Journal, 767:73 (15pp), 2013 April 10 doi:10.1088/0004-637X/767/1/73
© 2013. The American Astronomical Society. All rights reserved. Printed in the U.S.A.

# MID-INFRARED DETERMINATION OF TOTAL INFRARED LUMINOSITY AND STAR FORMATION RATES OF LOCAL AND HIGH-REDSHIFT GALAXIES

W. Rujopakarn[1], G. H. Rieke[1], B. J. Weiner[1], P. Pérez-González[1,2], M. Rex[1], G. L. Walth[1], and J. S. Kartaltepe[3]
[1] Steward Observatory, The University of Arizona, Tucson, AZ 85721, USA; wiphu@as.arizona.edu
[2] Universidad Complutense de Madrid, Facultad de Ciencias Físicas Dpto, de Astrofísica y CC, de la Atmósfera Madrid E-28040, Spain
[3] National Optical Astronomy Observatory, 950 North Cherry Avenue, Tucson, AZ 85719, USA
*Received 2012 November 14; accepted 2013 February 21; published 2013 March 26*

## ABSTRACT

We demonstrate estimating the total infrared luminosity, $L$(TIR), and star formation rates (SFRs) of star-forming galaxies at redshift $0 < z < 2.8$ from single-band 24 $\mu$m observations, using local spectral energy distribution (SED) templates without introducing additional free parameters. Our method is based on characterizing the SEDs of galaxies as a function of their $L$(TIR) surface density, which is motivated by the indications that the majority of IR luminous star-forming galaxies at $1 < z < 3$ have extended star-forming regions, in contrast to the strongly nuclear concentrated, merger-induced starbursts in local luminous and ultraluminous IR galaxies. We validate our procedure for estimating $L$(TIR) by comparing the resulting $L$(TIR) with those measured from far-IR observations, such as those from *Herschel* in the Extended Chandra Deep Field South (ECDFS) and Hubble Deep Field North (HDFN), as well as $L$(TIR) measured from stacked far-IR observations at redshift $0 < z < 2.8$. Active galactic nuclei were excluded using X-ray and 3.6–8.0 $\mu$m observations, which are generally available in deep cosmological survey fields. The Gaussian fits to the distribution of the discrepancies between the $L$(TIR) measurements from single-band 24 $\mu$m and *Herschel* observations in the ECDFS and HDFN samples have $\sigma < 0.1$ dex, with ∼10% of objects disagreeing by more than 0.2 dex. Since the 24 $\mu$m estimates are based on SEDs for extended galaxies, this agreement suggests that ∼90% of IR galaxies at high $z$ are indeed much more physically extended than local counterparts of similar $L$(TIR), consistent with recent independent studies of the fractions of galaxies forming stars in the *main-sequence* and *starburst* modes, respectively. Because we have not introduced empirical corrections to enhance these estimates, in principle, our method should be applicable to lower luminosity galaxies. This will enable use of the 21 $\mu$m band of the Mid-Infrared Instrument on board the *James Webb Space Telescope* to provide an extremely sensitive tracer of obscured SFR in individual star-forming galaxies across the peak of the cosmic star formation history.

*Key words:* galaxies: evolution – galaxies: high-redshift – infrared: galaxies

*Online-only material:* color figures

## 1. INTRODUCTION

The mid-infrared (mid-IR) is a unique window to study the evolution of star-forming galaxies, especially at redshift $1 < z < 3$ where the cosmic star formation rate (SFR) peaks (e.g., Hopkins & Beacom 2006). At these redshifts, a majority of star formation took place in obscured environments, where dust reprocesses the UV photons from hot young stars into IR emission (see e.g., Le Floc'h et al. 2005; Pérez-González et al. 2005; Dole et al. 2006; Buat et al. 2007). Star-forming galaxies at these redshifts also exhibit a large spread of extinction values and diverse dust distribution scenarios (Rujopakarn et al. 2012). These factors pose inherent challenges for optical and UV estimators of the SFR, which need to be complemented by IR techniques.

In the past decade, *ISO*, *Spitzer*, *WISE*, *AKARI*, and *Herschel* have allowed us to study star formation from the local universe out to high $z$ using mid-IR and far-IR observations. Measurements that determine the IR luminosity, $L$(TIR), from these missions trace the energy absorbed from UV photons emitted by short-lived massive stars (see, e.g., Kennicutt 1998). The most direct approach to measure $L$(TIR) is to use multi-band mid- and far-IR photometry. Recent examples use *Herschel* to observe star-forming galaxies at 100–500 $\mu$m and fit galaxy spectral energy distributions (SEDs) to measure $L$(TIR) (e.g., Elbaz et al. 2010; Rex et al. 2010; Elbaz et al. 2011). The complete characterization of the spectral peak of the dust emission provides a good measurement of $L$(TIR) and SFR. However, the inherent requirement of multi-band photometry for far-IR SED fitting compromises this approach for faint galaxies whose detection is limited by confusion noise, particularly at the longer wavelengths (e.g., Condon 1974; Dole et al. 2004). A second approach is to use a monochromatic (single-band) IR luminosity to trace $L$(TIR) and SFR. Locally, the rest-frame single-band 24 $\mu$m luminosity has been shown to be one of the best tracers for $L$(TIR) and SFR (Calzetti et al. 2007; Rieke et al. 2009). Although the longer wavelengths, such as 70 $\mu$m and 160 $\mu$m, are closer to the peak of the thermal dust emission and thus reduce the size of the bolometric corrections, they are affected more by the cold dust heated by old stars, which increases scatter in the SFR calibration compared to estimates from 24 $\mu$m (Rieke et al. 2009; Kennicutt et al. 2009), particularly in less luminous IR galaxies (Calzetti et al. 2010).

Beyond the local universe, however, the redshifted 24 $\mu$m band probes wavelengths containing the aromatic emissions (e.g., polycyclic aromatic hydrocarbons, hereafter PAHs); the strongest PAH emission complexes at 6.2, 7.7, and 8.6 $\mu$m (e.g., Smith et al. 2007) redshift into the 24 $\mu$m band by $z \sim 2$. Although they help boost the 24 $\mu$m flux and aid detection of galaxies at high $z$, PAHs pose two challenges to using single-band 24 $\mu$m observations to estimate $L$(TIR) and SFR. First, the PAH emission is influenced by environment (e.g., UV radiation, optical depth), introducing a ∼0.2 dex scatter to the $L$(TIR) and SFR estimates (Roussel et al. 2001). Second, the PAH emission

appears to strengthen intrinsically at high $z$ compared to that found in local galaxies with the same $L$(TIR) (Rigby et al. 2008; Farrah et al. 2008; Takagi et al. 2010). Therefore, the bolometric corrections to determine $L$(TIR) measured from local galaxies in the PAH wavelength regions will not be applicable at high $z$. Recent studies indicate that applying the local bolometric corrections to high-$z$ galaxies will overestimate their $L$(TIR) and SFR by up to an order of magnitude. This is reported as the "mid-IR excess" in recent far-IR studies using *Spitzer* and *Herschel* (e.g., Papovich et al. 2007; Elbaz et al. 2010; Nordon et al. 2010, 2012; Barro et al. 2011). The SED evolution causes a *systematic bias* that must be taken into account to use 24 $\mu$m observations as $L$(TIR) and SFR indicators beyond the local universe.

Out to $z \sim 3$, the *Spitzer* 24 $\mu$m observations probe weaker SFR at any given redshift than is possible with the far-IR bands (see Figure 4 of Elbaz et al. 2011). For the *James Webb Space Telescope*, 21 $\mu$m is the longest wavelength band suitable for deep cosmological surveys. Therefore, our understanding of star-forming galaxies at high $z$ will depend critically on mid-IR SFR indicators, where the current state-of-the-art prescription to estimate $L$(TIR) from single-band 24 $\mu$m observations still presents a 0.4 dex scatter (Nordon et al. 2012). Additionally, the *Spitzer* 24 $\mu$m data are already available from deep legacy surveys (e.g., GOODS, FIDEL, COSMOS, SpUDS), as well as from large-area surveys (e.g., SWIRE and the Boötes field) that will not be fully surveyed by current facilities to the same depth in terms of SFR. Exploration of means to reduce the current 0.4 dex scatter in $L$(TIR) estimates will allow utilization of the mid-IR observations to the fullest extent in the upcoming decade.

In this paper, we apply the results from our previous study, Rujopakarn et al. (2011), to take into account the SED evolution of star-forming galaxies and refine the 24 $\mu$m $L$(TIR) and SFR indicators. Rujopakarn et al. (2011) find that the IR luminosity surface density, $\Sigma_{L(\mathrm{TIR})}$, affords an accurate description of the SED and subsequently allows accurate bolometric corrections out to high $z$, specifically out to $z = 2.8$, the farthest redshift where the *Spitzer* 24 $\mu$m band traces predominantly PAH emissions. The measurement of $\Sigma_{L(\mathrm{TIR})}$ requires high-resolution imaging of the star-forming regions, which is only available for a small number of galaxies. We use these galaxies as a tool to construct a simple formula to estimate $L$(TIR) and SFR without measuring $\Sigma_{L(\mathrm{TIR})}$ for individual galaxies and using only single-band 24 $\mu$m flux and redshift measurements, and then compare the resulting $L$(TIR) estimates with results using far-IR data.

This paper is organized as follows. We discuss the evolution of the SEDs of star-forming galaxies and the use of $\Sigma_{L(\mathrm{TIR})}$ as a guide to select the appropriate SED for high-$z$ galaxies in Section 2. The derivation of the single-band $L$(TIR) indicator is described in Section 3. We then compare the new $L$(TIR) indicator with other independent measurements in Section 4 and present the $L$(TIR) SFR indicator in Section 5. Last, we discuss the validity of rest-frame 8–24 $\mu$m as a tracer of $L$(TIR) and SFR, along with implications of our results in Section 6. Throughout this paper, we assume a $\Lambda$CDM cosmology with $\Omega_m = 0.3$, $\Omega_\Lambda = 0.7$, and $H_0 = 70$ km s$^{-1}$ Mpc$^{-1}$. We follow the convention of Rieke et al. (2009) and adopt the definition of $L$(TIR) of Sanders & Mirabel (1996); these studies defined $L$(TIR) slightly differently (i.e., 5–1000 $\mu$m versus 8–1000 $\mu$m), but the resulting $L$(TIR) values are closely consistent. We will refer to galaxies with $L$(TIR) in the range of $10^{11}$–$10^{12}$ and those with $L(\mathrm{TIR}) > 10^{12}\,L_\odot$ as Luminous Infrared Galaxies (LIRGs) and Ultraluminous Infrared Galaxies (ULIRGs), respectively, or collectively as U/LIRGs.

## 2. QUANTIFYING THE IR SED EVOLUTION

In this section, we will discuss the challenges in using *Spitzer* observations at 24 $\mu$m to estimate $L$(TIR) and SFR. Major issues are to determine an overall approach for using $\Sigma_{L(\mathrm{TIR})}$ as an indicator of a galaxy SED (Section 2.1), and the choice of SED library (Section 2.2).

### 2.1. $\Sigma_{L(\mathrm{TIR})}$ as an Indicator of SEDs for Star-forming Galaxies

Until now, most estimations of the $L$(TIR) and SFR of galaxies using single-band IR observations rely on an assumption that the SED of a star-forming galaxy does not evolve with redshift, i.e., that bolometric corrections measured from local SED templates can be applied to high-$z$ galaxies. However, local IR galaxies, from which we construct the SED libraries, comprise an inhomogeneous population of both normal star-forming galaxies (quiescent disks) and those with nuclear star formation induced by galaxy interactions. The contribution of interaction-induced star formation increases with $L$(TIR); locally, theoretical studies suggest that ULIRGs must be dominated by interaction-induced starbursts to achieve their $L$(TIR) outputs (Hopkins et al. 2010), which is consistent with observations (e.g., Sanders & Mirabel 1996; Veilleux et al. 2002). The application of local bolometric corrections to high-$z$ galaxies thus carries an implicit assumption that high-$z$ star-forming galaxies are likewise dominated by interaction-induced starbursts.

Observations have shown, however, that actively star-forming galaxies at high $z$ are different from their local counterparts in at least three major aspects. First, the IR SEDs at high $z$ exhibit colder far-IR dust temperatures, $T_d$, than local galaxies at fixed $L$(TIR) (Pope et al. 2006; Symeonidis et al. 2009; Muzzin et al. 2010). These galaxies have dust temperatures similar to local galaxies with lower $L$(TIR). Second is the aforementioned evolution of the strength of the aromatic features, which grow stronger at high $z$ at a fixed $L$(TIR). Quantitatively, for instance, Rigby et al. (2008) found A2218a, a galaxy with $L$(TIR) of $10^{11.9}\,L_\odot$ at $z = 2.5$, to exhibit aromatic emission features virtually identical to those of a local galaxy with an order of magnitude lower $L$(TIR).

Third, Rujopakarn et al. (2011) found that the diameters of the galactic-wide star-forming regions in high-$z$ U/LIRGs are 10–30 times larger than those of local U/LIRGs at the same $L$(TIR). The size of the star-forming regions found in high-$z$ U/LIRGs is similar to that of local normal star-forming galaxies (sub-LIRG), 4–10 kpc in diameter, but with $\Sigma_{\mathrm{SFR}}$ scaled up by a factor of 100–1000 (Figures 3 and 4 of Rujopakarn et al. 2011). This structural similarity is a manifestation of the "main sequence" of star-forming galaxies, originally defined as a sequence of galaxies in stellar mass versus SFR space (Noeske et al. 2007), where star-formation occurs at a relatively steady rate rather than in bursts, and in disks or clumps, rather than in merger nuclei (e.g., Genzel et al. 2010; Tacconi et al. 2010; Narayanan et al. 2011; Daddi et al. 2010; Elbaz et al. 2010, 2011). In its simplest form, this picture suggests that these galaxies differ among themselves (and from local lower luminosity star-forming galaxies) primarily in the SFR surface density, $\Sigma_{\mathrm{SFR}}$, and hence in IR luminosity surface density, $\Sigma_{L(\mathrm{TIR})}$.

In Figure 1, adapted from Figure 4 of Rujopakarn et al. (2011), we show $\Sigma_{L(\mathrm{TIR})}$ as a function of $L$(TIR) along with

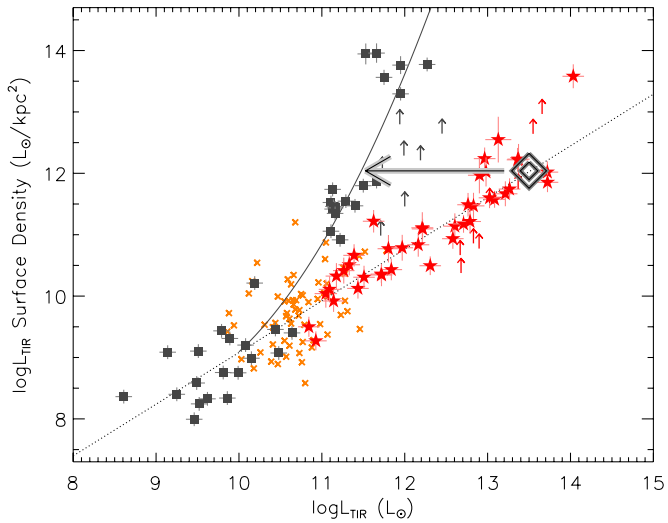


**Figure 1.** The relationships between the $L$(TIR) and $L$(TIR) surface density, $\Sigma_{L(\mathrm{TIR})}$, differ for the local and non-local galaxies (gray squares and red stars, respectively). Local galaxies from Chanial et al. (2007) are shown for comparison as orange crosses. The upward arrows represent points derived from CO size measurements, which could be systematically more extended than the other size tracers employed (Rujopakarn et al. 2011) and thus are taken as lower limits in $\Sigma_{L(\mathrm{TIR})}$. The solid and dashed lines are the fits for local and high-$z$ galaxies (excluding the CO lower limits), respectively. Rujopakarn et al. (2011) show that the SEDs of galaxies are to first order indicated solely by their $\Sigma_{L(\mathrm{TIR})}$. For example, a high-$z$ galaxy with $L$(TIR) of $10^{13.5}\,L_\odot$ will have aromatic emissions and absorption features consistent with a local galaxy with the same $\Sigma_{L(\mathrm{TIR})}$, indicated by the arrow, in this case a local galaxy with $L$(TIR) of $\sim 10^{11.5}\,L_\odot$ (see Section 3). This behavior, plus the tendency of the great majority of high-$z$ galaxies to lie near the main sequence, allows a simple approach to associating the appropriate SED with typical high-$z$ galaxies.

(A color version of this figure is available in the online journal.)

trend lines describing the relationship in each population, one for local galaxies with $L$(TIR) above $10^{11}\,L_\odot$ and another for high-$z$ galaxies. The main sequence can be drawn in this figure from the local normal star-forming galaxies (sub-LIRG galaxies) onto the high-$z$ star-forming galaxies. Both the local and high-$z$ relationships agree below $L(\mathrm{TIR}) \sim 10^{11}\,L_\odot$. The trends diverge above the LIRG threshold, where the local galaxy sample starts to be dominated by galaxies harboring interaction-induced star formation (see also Totani et al. 2011 for the local relationship).

Rujopakarn et al. (2011) estimated $\Sigma_{L(\mathrm{TIR})}$, defined by $\Sigma_{L(\mathrm{TIR})} = L(\mathrm{TIR})/A$, by measuring the area, $A$, of the IR-emitting region using radio continuum (e.g., 1.4 GHz), Paschen-$\alpha$, and 24 $\mu$m observations. Although the emission physics of these size measures is different, they trace a consistent physical extent of the star-forming regions and are similarly insensitive to contributions from old stellar populations. Paschen-$\alpha$ and 24 $\mu$m are the two best IR tracers of SFR and are emitted from approximately the same spatial extent. Also, Chanial et al. (2007) found that radio continuum (e.g., 1.4 GHz) and far-IR size measurements are consistent within 15%. For the purpose of determining the surface area of star formation in individual galaxies, we will thus use these three size tracers interchangeably. Among these indicators, only the interferometric observation of the radio synchrotron continuum can resolve individual galaxies at high-$z$. The main sample of high-$z$ galaxies in Figure 1 was therefore from the Muxlow et al. (2005) 1.4 GHz VLA+MERLIN survey of the Hubble Deep Field with angular resolution of 0.″2–0.″5. This is a blind survey that has resolved all of the 92 detected galaxies, which ensures that the extended physical sizes at high $z$ are not due to selection bias. The Muxlow et al. sample is augmented by radio observations of sub-mm galaxies from the literature with similarly high angular resolutions. The samples of galaxies with physical size measurements are provided in Tables 4 and 5 for interested readers.

Following the Rujopakarn et al. (2011) example, the use of $\Sigma_{L(\mathrm{TIR})}$ as an indicator of SED characteristics can be illustrated by envisioning a horizontal line at a fixed $\Sigma_{L(\mathrm{TIR})}$ in Figure 1. As an example, if we assume the $z = 2.5$ A2218a with $L$(TIR) of $10^{11.9}\,L_\odot$, observed by Rigby et al. (2008), is located on the main-sequence, we would expect it to exhibit spectral characteristics of a galaxy on the local sequence with $L$(TIR) of $\sim 10^{10.9} L_\odot$ that has the same $\Sigma_{L(\mathrm{TIR})}$. Rujopakarn et al. (2011) further demonstrate the ability of $\Sigma_{L(\mathrm{TIR})}$ to predict SED behavior by predicting the 24 $\mu$m-to-1.4 GHz flux ratios, which are sensitive to PAH features at $z \sim 2$, consistent with the observed ratios (their Figure 5), as well as matching the average observed aromatic spectrum of high-$z$ ULIRGs to a local SED template (their Figure 7). The assumption that $\Sigma_{L(\mathrm{TIR})}$ is the dominant parameter controlling the average SED thus provides a tool to assign an appropriate local SED template to represent the SED of high-$z$ galaxies, a result we will use to construct an indicator for $L$(TIR) and SFR in this work.

The $\Sigma_{L(\mathrm{TIR})}$ method is physically motivated because the PAH emission emerges from the outer surfaces of the photodissociation regions (PDRs; e.g., Tielens 2008), so the surface density of the SFR is a controlling factor for the PAH-emitting surface area and thus the PAH emission strength. Additionally, Chakrabarti & McKee (2005) modeled the radiative transfer in centrally heated dusty sources and found a general relation among the luminosity-to-mass ratio, the surface density, and the shape of the SED. They predict that the behavior of SED templates for local galaxies might not extend to high $z$. Extended sizes and colder SEDs were also shown to be connected through a $T_d$–$\Sigma_{L(\mathrm{TIR})}$ relation explored by Chanial et al. (2007), who theoretically described the IR-emitting region of a star-forming galaxy as an isothermal cloud optically thick to optical wavelengths and optically thin in the IR. Chanial et al. (2007) show that $L$(TIR), $T_d$, and the extent of the IR-emitting region are related by a fundamental plane; the $L$(TIR)–$T_d$ relation (e.g., Soifer et al. 1987) is a manifestation thereof.

### 2.2. The Local Reference for the Galaxy SEDs

The SED libraries commonly used to represent the spectra of star-forming galaxies are those of, e.g., Chary & Elbaz (2001), Dale & Helou (2002), and Rieke et al. (2009). The former two libraries were based on spectra taken by *ISO*, preceding the availability of full spectral coverage at 6–24 $\mu$m (that the 24 $\mu$m band probes at redshift $z = 2.8$–0). The recent infrared spectrograph (IRS) observations from *Spitzer*, covering 5.2–38 $\mu$m, show that the Chary & Elbaz (2001, hereafter CE01) SED templates have suppressed aromatic features at very high luminosity (Chary & Pope 2010) and do not sufficiently take into account the strong silicate absorption features at 10 $\mu$m, resulting in weaker aromatic bands but stronger net emission in the PAH-region comparing to observed galaxies (Armus et al. 2007; Rieke et al. 2009). The Dale & Helou (2002) SED library is optimized to describe moderately-luminous local star-forming galaxies with $L(\mathrm{TIR}) < 10^{11}\,L_\odot$ and hence the lack of silicate absorption in these templates becomes more significant at higher $L$(TIR) with larger typical extinction.

Rieke et al. (2009, hereafter R09) developed SED templates, which we adopt as the SED reference for local galaxies,

separately for normal star-forming galaxies (sub-LIRG) and U/LIRGs to provide a self-consistent SED library covering $L$(TIR) of $10^{9.75}$ to $10^{13.00}$ $L_\odot$. The U/LIRGs SED templates were constructed from a sample of 11 local LIRGs and ULIRGs with high quality *Spitzer*/IRS spectra as well as photometric data covering optical to radio wavelengths (see Figures 1, 2, and 3 of Rieke et al. 2009). These U/LIRGs were chosen such that their IR emission is dominated by star-forming activity. Construction of the SED library is done in two steps. First, these 11 galaxies were used as a basis to assemble 11 archetypal SED templates spanning 0.4 $\mu$m to 30 cm wavelength. Their IRS spectra (5–38 $\mu$m) were joined to the photospheric emission and far-IR dust emission components in a series of tests to ensure both spectral continuity and appropriate flux calibration. Second, these archetypal templates were combined with different weights to produce the final averaged SED templates. The template weights were optimized by matching synthesized IR colors from the combined template to the average IR colors of observed galaxies as a function of $L$(TIR) from IRAC and the *IRAS* RBGS (Sanders et al. 2003). The R09 library construction was extended to star-forming galaxies with sub-LIRG $L$(TIR) by combining the Dale & Helou (2002) SED library with the mid-IR spectral library based on IRS observations from Smith et al. (2007) using the same IR color fitting technique as in the U/LIRG template construction. The use of IR color to help guide the combination of archetypal templates (i.e., fitting 25/8 $\mu$m, 25/12 $\mu$m, and 60/25 $\mu$m colors simultaneously) helps ensure that the final templates represent the average properties of real galaxies even though they are constructed from a limited sample. The R09 SED library construction is described in detail in the Appendix of Rieke et al. (2009). We adopt these templates for this paper.

## 3. A MID-IR ESTIMATOR FOR $L$(TIR) AT $0 < z < 2.8$

The construction of a 24 $\mu$m SFR indicator has two steps: (1) construct an $L$(TIR) estimator using 24 $\mu$m flux and redshift, and then (2) derive a relationship between $L$(TIR) and SFR. The first step would appear to require measuring $\Sigma_{L(\mathrm{TIR})}$ for each galaxy to determine the appropriate SED template. However, the relatively small scatter of the high-$z$ galaxies around the main sequence in Figure 1 suggests that adequate SED template matching can be achieved by assuming a typical surface area. In this section, we will use the sample with $\Sigma_{L(\mathrm{TIR})}$ measurements in Figure 1 to construct a formula that can be applied to estimate SFRs in the absence of the physical size measurements.

Rieke et al. (2009) first assign a value of $L$(TIR) to each SED template and then determine the corresponding SFR as well as the monochromatic luminosity through the desired bandpasses. For the 24 $\mu$m band, in particular, the assignment of the 24 $\mu$m luminosity of a template follows the ratio of $L(24\,\mu\mathrm{m})$-to-$L$(TIR) based on the local *IRAS* data (see Figures 8 and 15 and formula A6 of Rieke et al. 2009). Once each template has an associated 24 $\mu$m luminosity, it is possible to calculate the $k$-corrections and subsequently the expected monochromatic flux for each template as a function of redshift. For $L_\nu \propto \nu f_\nu$, the $k$-correction, $K_{\mathrm{corr}}(z)$, and the flux, $f_\nu(24\,\mu\mathrm{m})$, are related by

$$K_{\mathrm{corr}}(z) = (1+z)\frac{f_\nu(\nu = (1+z)\nu_{\mathrm{obs}})}{f_\nu(24\,\mu\mathrm{m})} \quad (1)$$

$$4\pi\, {D_L}^2 f_{\nu,\mathrm{obs}} = \frac{L_{\nu,\mathrm{rest}}(24\,\mu\mathrm{m})}{\nu_{24}} K_{\mathrm{corr}}(z) \quad (2)$$

where $D_L$ is the luminosity distance for an object at redshift $z$. The $4\pi\, {D_L}^2 f_{24,\mathrm{obs}}$ for this equation has the units of Jy cm$^2$. The relationship between the observed monochromatic flux from each template and the template's monochromatic luminosity at a given redshift is approximately linear, which allows for a linear fit at each redshift (i.e., for a redshift grid) to determine a set of coefficients that convert the observed flux at a given redshift to the luminosity or any quantity associated with the template (e.g., $L$(TIR) and SFR). For example, a relationship between $L$(TIR) and the observed 24 $\mu$m flux, $f_{24,\mathrm{obs}}$, has the form

$$\log L(\mathrm{TIR})_{z=0} = A(z) + B(z)\left[\log\left(4\pi\, {D_L}^2 f_{24,\mathrm{obs}}\right) - C\right], \quad (3)$$

where $A(z)$ and $B(z)$ are the intercept and the slope from the linear fit, respectively, $C$ is a zero-point to reduce covariance in the fit parameters, and $L(\mathrm{TIR})_{z=0}$ refers to the $L$(TIR) associated with each of the R09 SED templates. Rieke et al. (2009) use this method to tabulate the coefficients to convert the monochromatic fluxes in various bands to the SFR of galaxies.

This formalism successfully estimates $L$(TIR) and SFR for local galaxies. However, a modification is needed to apply the formalism at high $z$ (Rieke et al. 2009). If we assume that IR star-forming galaxies beyond the local universe are in the main sequence (we discuss the validity and applicability of this assumption in Section 6.2), it is possible to use the corresponding $\Sigma_{L(\mathrm{TIR})}$ as a guide to estimate $L$(TIR) and SFR at high $z$ without the need for $\Sigma_{\mathrm{SFR}}$ measurements of individual galaxies. Following Rujopakarn et al. (2011), an appropriate choice of SED to use for calculations of the $k$-correction and bolometric correction beyond the local universe is the one corresponding to the same $\Sigma_{L(\mathrm{TIR})}$ locally. This is equivalent to reassigning the $L$(TIR) associated with each of the R09 SED templates to new values determined by the ratio of luminosities with equal $\Sigma_{L(\mathrm{TIR})}$ on the local U/LIRG trend to those on the main sequence. We will refer to this ratio as the *stretching factor*, $S_i$, for each SED template. From Figure 1, $S_i$ is nearly negligible at $L(\mathrm{TIR})_{z=0} = 10^{11}$ $L_\odot$ and reaches three orders of magnitude at $L(\mathrm{TIR})_{z=0}$ of $10^{14}$ $L_\odot$. To determine $S_i$ quantitatively, we parameterize the relationship by fitting a parabola to the local U/LIRG relation (excluding the lower limits of $\Sigma_{L(\mathrm{TIR})}$ from CO observations) and a linear fit to the main sequence, and then take the ratio of $L$(TIR) on the main sequence fit to the R09 template $L$(TIR) at the same $\Sigma_{L(\mathrm{TIR})}$ (see Figure 1; the $S_i$ values are tabulated in Table 1). Since we effectively increase the luminosity of each template by a factor of $S_i$, the observed flux will also be increased by the same factor. Equation (3) can thus be rewritten as

$$\begin{aligned}\log L(\mathrm{TIR})_{\mathrm{new}} &= \log[S_i\, L(\mathrm{TIR})_{z=0}] \\ &= A'(z) + B'(z)\left[\log\left(4\pi\, {D_L}^2 S_i\, f_{24,\mathrm{obs}}\right) - C'\right].\end{aligned} \quad (4)$$

The new set of coefficients, $A'(z)$, $B'(z)$, and $C'$, can be determined by re-fitting Equation (4). We have limited the fitting range to only encompass the "stretched" luminosity of $\log L(\mathrm{TIR})_{\mathrm{new}} < 14$ because the stretched luminosities at large $S_i$ are far greater than the luminosity range occupied by real galaxies (the $10^{14}$ $L_\odot$ cut off is chosen because we expect this to be approximately at luminosity limit of star-forming galaxies). For a given template, the shape as a function of redshift remains the same. The effect of the $S_i$ is to change the spacing between templates. The relationship between luminosity and observed flux remains well approximated as linear, with residuals <0.05 dex.

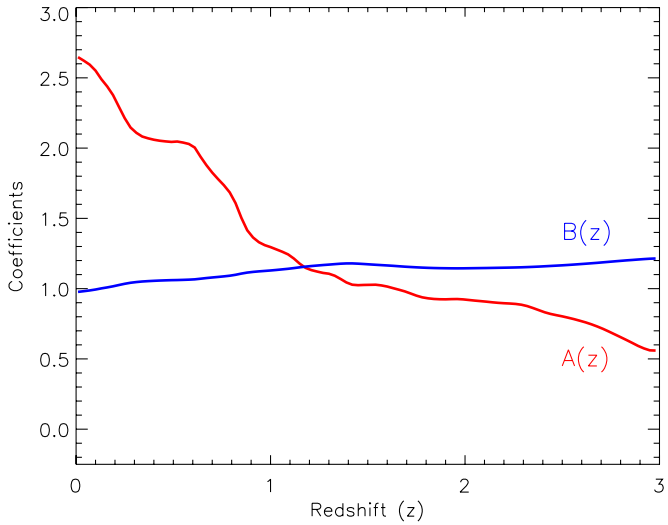


**Figure 2.** The coefficients of the fits for a relationship between the observed *Spitzer* 24 $\mu$m flux and the total IR luminosity (Equation (5)) as a function of redshift. The coefficients $A'(z)$ and $B'(z)$ are shown by the red and blue lines. These coefficients are tabulated in Table 2.

(A color version of this figure is available in the online journal.)

**Table 1**
Stretching Factors and $L(\mathrm{TIR})_{\mathrm{new}}$ Associated with Rieke et al. (2009) SED Templates

| $\log L(\mathrm{TIR})_{z=0}$ [a] | $\log S_i$ | $\log L(\mathrm{TIR})_{\mathrm{new}}$ |
|---|---|---|
| 9.75 | −0.118 | 9.63 |
| 10.00 | 0.013 | 10.01 |
| 10.25 | 0.173 | 10.42 |
| 10.50 | 0.408 | 10.91 |
| 10.75 | 0.717 | 11.47 |
| 11.00 | 1.101 | 12.10 |
| 11.25 | 1.560 | 12.81 |
| 11.50 | 2.095 | 13.59 |
| 11.75 | 2.704 | 14.45 |
| 12.00 | 3.388 | 15.39 |

**Notes.** Column 1: original $L$(TIR) associated to each of the Rieke et al. (2009) SED templates; Column 2: stretch factors from the fit to the $L$(TIR)–$\Sigma_{L(\mathrm{TIR})}$ relationship of local galaxies (Section 3); Column 3: resulting $L(\mathrm{TIR})_{\mathrm{new}}$ associated to SED template shape from the fit.

[a] The Rieke et al. (2009) SED templates with $L(\mathrm{TIR})_{z=0} > 10^{12}\ L_\odot$ are omitted because their $L(\mathrm{TIR})_{\mathrm{new}}$ are higher than luminosities of observed galaxies. These SED template shapes are thus unlikely to represent real galaxies at high $z$.

The fitting coefficients, $A'(z)$ and $B'(z)$, to relate the observed *Spitzer* 24 $\mu$m flux to $L$(TIR) as a function of redshift, are shown in Figure 2 (as dotted lines) and tabulated in Table 2. The relation is

$$\log L(\mathrm{TIR})_{\mathrm{new}} = A'(z) + B'(z)\left[\log\left(4\pi D_L{}^2 f_{24,\mathrm{obs}}\right) - 45\right]. \quad (5)$$

Apart from the 24 $\mu$m single-band $L$(TIR) indicator, we also use the local $L$(TIR)–$\Sigma_{\mathrm{SFR}}$ relationship to derive the $A(z)$ and $B(z)$ coefficients to estimate $L$(TIR) from the 70 $\mu$m observed flux (e.g., *Spitzer*/MIPS or *Herschel*/PACS). The resulting coefficients yield single-band 70 $\mu$m $L$(TIR) consistent with the values from the original Rieke et al. (2009) estimator at $L(\mathrm{TIR}) < 10^{11}\ L_\odot$ and overestimate the Rieke et al. (2009) $L$(TIR) by <0.15 dex at higher luminosities. We do not anticipate strong evolution of the SED in the rest-frame wavelength range probed by the observed 70 $\mu$m band at redshift $z = 0$–2.8 (70–18.4 $\mu$m) because it is still in the dominant blackbody emission peak, unlike the 24 $\mu$m band. Thus the Rieke et al. (2009) coefficients can be used to estimate $L$(TIR) and SFR from 70 $\mu$m observations.

**Table 2**
Coefficients of the Fits for the Relation between *Spitzer* 24 $\mu$m Flux and the $L$(TIR)

| $z$ | $A'(z)$ | $B'(z)$ |
|---|---|---|
| 0.0 | 2.656 | 0.975 |
| 0.2 | 2.350 | 1.020 |
| 0.4 | 2.060 | 1.056 |
| 0.6 | 2.012 | 1.065 |
| 0.8 | 1.659 | 1.094 |
| 1.0 | 1.296 | 1.129 |
| 1.2 | 1.137 | 1.159 |
| 1.4 | 1.039 | 1.179 |
| 1.6 | 1.015 | 1.165 |
| 1.8 | 0.934 | 1.149 |
| 2.0 | 0.922 | 1.145 |
| 2.2 | 0.896 | 1.149 |
| 2.4 | 0.837 | 1.158 |
| 2.6 | 0.768 | 1.175 |
| 2.8 | 0.655 | 1.198 |

**Note.** $A'(z)$ and $B'(z)$ are the coefficients for Equation (5).

## 4. TESTING THE NEW 24 $\mu$m $L$(TIR) INDICATOR

We test the new 24 $\mu$m indicator on seven samples of galaxies with far-IR $L$(TIR) measurements. Five of these samples are of individual galaxies; two are stacked multi-band far-IR photometry. In Section 4.1, we test the indicator on individual galaxies with accurate far-IR photometry from *Herschel* to establish that the method can successfully estimate $L$(TIR) of star-forming galaxies without systematic biases, as well as to quantify the scatter of $L$(TIR) estimates for individual galaxies. Individual gravitationally lensed galaxies at $1.0 < z < 2.7$ with far-IR and sub-mm $L$(TIR) measurements are also introduced in this section to test the indicator down to the LIRG regime at $z \gtrsim 2$. In Section 4.2, we test the applicability of the indicator using averaged SEDs (i.e., stacked) of a wide range of star-forming galaxies in cosmological surveys at $0 < z < 2.8$. Additionally, we verify the uncertainty estimate of the $L$(TIR) values using an independent sample of individual galaxies that have *Spitzer* far-IR observations and photometric redshifts in Section 4.3.

### *4.1. Testing the 24 $\mu$m $L$(TIR) Indicator with Far-IR $L$(TIR) Measurements for Individual Galaxies*

The individual galaxies we use to verify that the new indicator predicts $L$(TIR) consistent with that from far-IR SED fitting are from the following: (1) *Herschel*/SPIRE observations of galaxies in the Extended Chandra Deep Field South (ECDFS) with spectroscopic redshift measurements; (2) *Herschel*/PACS and SPIRE observations of galaxies in the Hubble Deep Field North (HDFN) with spectroscopic redshift measurements, augmented by photometric redshifts; (3) the *Herschel* Lensing Survey (HLS; Egami et al. 2010; Rex et al. 2010) sample at $0.4 < z < 2.7$; (4) 24 $\mu$m-bright lensed galaxies at $1 < z < 2.7$ studied by Rujopakarn et al. (2012). These far-IR data sets provide photometric measurements near the peak of dust emission spectrum that can be used as fiducial $L$(TIR) estimates, in addition to their multiwavelength ancillary data

for active galactic nucleus (AGN) identification. A range of $10^{11} < L(\mathrm{TIR})\ 10^{13} < L_{\odot}$ is represented.

#### 4.1.1. Extended Chandra Deep Field South Sample

For the ECDFS sample, we processed the archival *Herschel*/SPIRE observations at 250, 350, and 500 $\mu$m, following the method described in Kennicutt et al. (2011) to produce the final maps in each band using HIPE release 8.1 (SPIRE pipeline version 8.0.3287). The original observations were from the HerMES survey (PI: S. Oliver). Flux measurements on these maps were done with point-spread function (PSF) photometry using the DAOPHOT software (Stetson 1987) on the 24 $\mu$m prior positions from the FIDEL survey (C. Papovich 2012, private communication) with no re-centering allowed. We measure the positional offsets between the prior coordinates and those of the SPIRE maps by stacking SPIRE sources and fit a 2D Gaussian to measure the offset of the resulting centroid of the stacked PSF from the priors. These offsets, $\alpha = -3\farcs3, \delta = 0\farcs8$, were applied to the maps before performing PSF photometry. The large, 18″–36″, beams of *Herschel*/SPIRE presents blending issues: fluxes from nearby objects can contribute artificially to the objects of interest. We developed a criterion based on the 24 $\mu$m prior catalog to exclude the potentially blended objects in an unbiased manner. This method is described in the Appendix.

AGNs are excluded from this test by excluding galaxies with $L_{\mathrm{X}}[0.5\text{–}8.0\,\mathrm{keV}] > 10^{42}$ erg s$^{-1}$ and those exhibiting IR power-law SED (Donley et al. 2012), based on the *Chandra* X-ray and *Spitzer*/IRAC catalogs from Lehmer et al. (2005) and Damen et al. (2011), respectively. The requirement of these ancillary data to exclude AGNs makes our method most useful where deep 24 $\mu$m observations are accompanied by those of deep X-ray and/or mid-IR (e.g., *Spitzer*/IRAC). This is presently the case in every major cosmological deep field, and future deep observational programs will likely take place in these same fields (e.g., ECDFS, GOODS-N, EGS, COSMOS, UDS). Thus, future investigations will be able to exclude AGNs much as we have.

We combine the *Spitzer*/MIPS 24 and 70 $\mu$m catalog from FIDEL and our SPIRE catalog to measure the $L$(TIR) for galaxies in the ECDFS. We limit our sample to those that have high-quality spectroscopic redshifts from the Arizona CDFS Environment Survey (ACES) that has 5,080 secure redshifts ($Q = 3$ or 4; Cooper et al. 2012) to minimize the effects of redshift uncertainties. The far-IR $L$(TIR) in the ECDFS is measured by fitting the Rieke et al. (2009) SED library to the MIPS 24 and 70 $\mu$m and at least one SPIRE band. We redshift the SED library to the value determined by the spectroscopic redshift of each object and minimize the $\chi^2$ value over the ranges of SED templates and the normalization factors. We inspect each SED fit visually to ensure fitting quality. Given the significantly smaller uncertainties of the MIPS photometry compared to those from SPIRE (especially at 24 $\mu$m), we avoid the possibilities that too much weight could have been put on the MIPS 24 and 70 $\mu$m points by adding 3% uncertainties in quadrature to each data point. We experimented with adding up to 25% uncertainties in this way and found that the resulting $L$(TIR) values do not depend sensitively on the choice of uncertainties added. In the SED fitting, we require at least one data *Herschel* data point at a rest-frame wavelength >30 $\mu$m to be detected at S/N > 5. The final sample for SED fitting is selected at 250 $\mu$m flux >7 mJy, which yields 91 galaxies that passed all these criteria, in addition to the blending avoidance criteria (the Appendix). The final sample has redshifts ranging from 0.1–1.3 with a median redshift $z = 0.6$. The comparison between *Herschel* fiducial $L$(TIR) and those from the new single-band 24 $\mu$m indicator is shown in Figure 3.

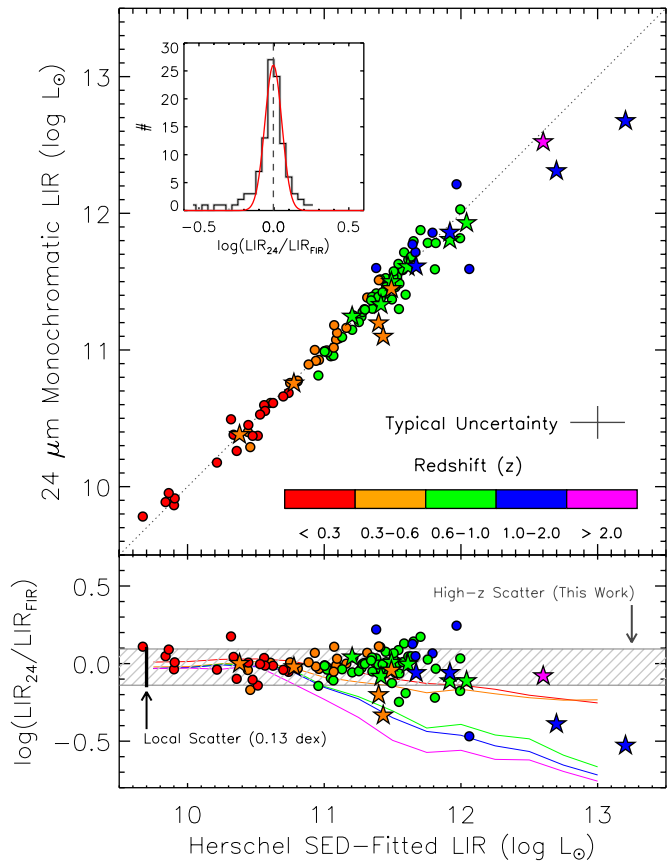


**Figure 3.** Comparison of $L$(TIR) derived from the new 24 $\mu$m indicator to $L$(TIR) measured by integrating the SED fitted to *Herschel*/SPIRE (250–500 $\mu$m) photometry for individual galaxies in the Extend Chandra Deep Field South (ECDFS) that have secure spectroscopic redshifts (circles); and in the *Herschel* Lensing Survey (HLS; stars). The bottom panel shows the ratio of $L$(TIR) from our single-band 24 $\mu$m indicator to the far-IR $L$(TIR). The overall scatter is 0.12 dex (shaded region), which is comparable to the scatter of the relationship between $L$(24 $\mu$m) and $L$(TIR) found locally (0.13 dex; illustrated by a vertical bar on the left). The lines in the bottom panel (color-coded by $z$) indicate the ratios that would result if the star-forming regions in high-$z$ IR galaxies were as compact as those found locally (i.e., if our extended structure assumption fails), which is the case for 6% of galaxies; each line corresponds to the upper-end of each $z$ bin in the top panel. The inset shows a Gaussian fit to the distribution, which has a $\sigma$ of 0.06 dex, indicating the degree of agreement where our extended structure assumption applies.

(A color version of this figure is available in the online journal.)

#### 4.1.2. Hubble Deep Field North Sample

For the HDFN sample, we gathered all the data obtained by *Herschel* in three different programs: the Guaranteed Time PACS Evolutionary Probe (PEP; PI: D. Lutz), the *Herschel* Multi-tiered Extragalactic Survey (HerMES, PI: S. Oliver), and the Open Time Key Program GOODS-*Herschel* (PI: D. Elbaz). All the PACS and SPIRE data taken by these surveys was downloaded from the *Herschel* Science Archive (HSA) and merged together using HIPE and proprietary dedicated software. The reduction steps were the standard for Level 2.0 and 2.5 data products in the HSA. Catalogs using MIPS 24 $\mu$m priors and direct detections were built using the procedure described in Pérez-González et al. (2010), which was conceived to extract

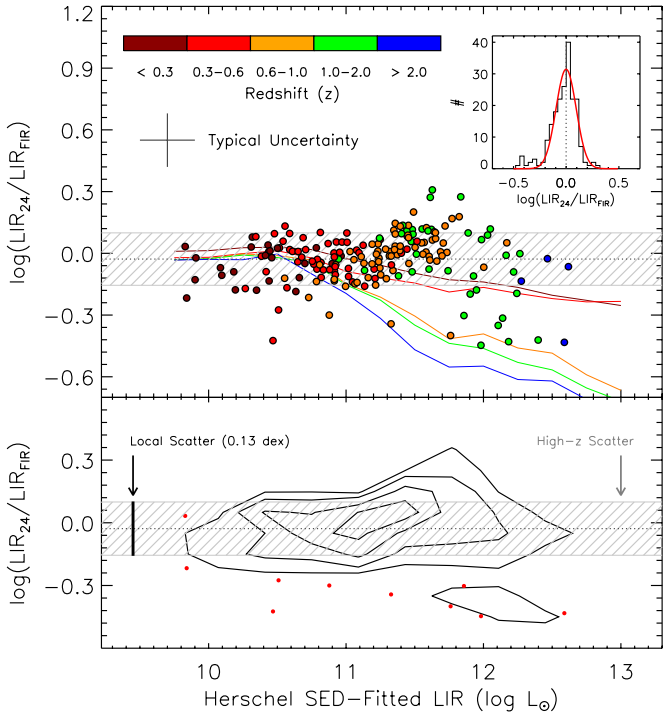


**Figure 4.** Comparison of $L$(TIR) estimates from the new 24 $\mu$m indicator to those measured with *Herschel*/PACS and SPIRE (100–500 $\mu$m) photometry in the Hubble Deep Field North. The top panel shows the ratio of $L$(TIR) from the 24 $\mu$m indicator to the far-IR $L$(TIR). The overall scatter is 0.13 dex (shaded region). Tracks representing ratios of compact objects, and the inset, are similar to those in Figure 3. The bottom panel shows the contours encompassing the top 25th, 50th, 75th, 90th percentiles of the distribution, along with outliers in red. Comparison of results here and those in Figure 3 indicates that the addition of the shorter wavelength far-IR data (e.g., 100–160) does not changed the result statistically, which demonstrates the general applicability of the indicator to far-IR-selected galaxies.

(A color version of this figure is available in the online journal.)

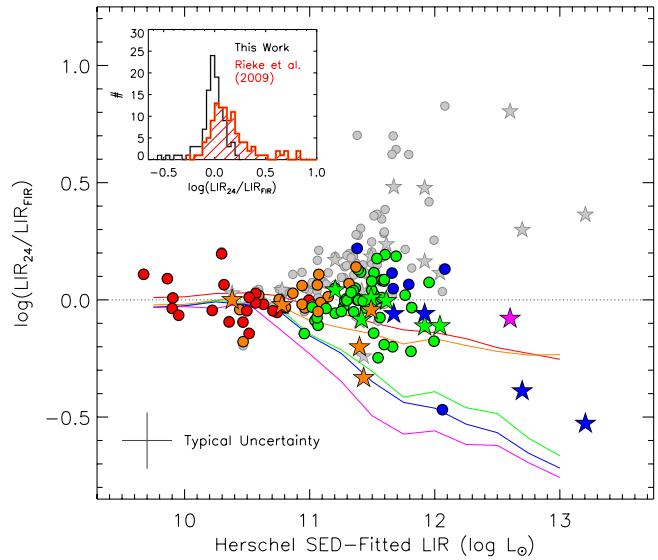


**Figure 5.** Same as Figure 3 but with the $L$(TIR) values from the Rieke et al. (2009) indicator shown as a comparison in gray. Color coding is identical to Figure 3 (color coding for the Rieke et al. indicator is omitted for clarity). The inset shows the histogram of the ratio, with values from the new indicator and those of Rieke et al. (2009) shown in black and red histograms, respectively. While the Rieke et al. (2009) indicator overestimates $L$(TIR) values compared to *Herschel* $L$(TIR), this overestimation and the "mid-IR excess problem" (Section 4.1) are shown to be alleviated by the new $L$(TIR) indicator.

(A color version of this figure is available in the online journal.)

fluxes from faint sources that are difficult to detect directly and to deblend nearby sources in the *Herschel* data (separated by more than 1 PSF FWHM for each band). The PACS catalogs reach 5$\sigma$ detections of 2 mJy at 100 $\mu$m, and 4 mJy at 160 $\mu$m. For SPIRE, the 5$\sigma$ level is at 10, 14, and 17 mJy for the 250, 350, and 500 $\mu$m bands, respectively. We compiled spectroscopic redshift measurements in the HDFN and augmented the sample with photometric redshift measurements (P. Pérez-González et al., in preparation) with accuracy of $\Delta z/(1+z) = 0.034$ based on a SED fitting process described in Barro et al. (2011). Two hundred galaxies in the HDFN are detected at S/N > 5 in at least one *Herschel* band longward of rest-frame 30 $\mu$m, passed the prior-based blending avoidance criteria (the Appendix), and do not harbor X-ray or IR power-law AGNs. Spectroscopic and photometric redshift measurements are available for 137 and 63 of these galaxies, respectively; the redshift range of the final sample is 0.06–2.21, with a median redshift $z = 0.7$. The $L$(TIR) comparison in HDFN is presented in Figure 4.

#### *4.1.3. Gravitationally Lensed Galaxies Samples*

The HLS sample consists of 19 galaxies located behind the Bullet Cluster at redshifts $0.4 < z < 3.24$ (Rex et al. 2010). These sources are detected in at least two *Herschel* bands (at 100–500 $\mu$m) and many are also observed in LABOCA 870 micron and AzTEC 1.1 mm maps of the field (Wilson et al. 2008; Johansson et al. 2010). These measurements tightly constrain the peak of the far-IR SED and therefore provide accurate estimates of $L$(TIR). We have excluded three galaxies from the original HLS sample (Table 2 of Rex et al. 2010) in our test: HLS12 and HLS13 ($z = 3.24$ and 2.9) because 24 $\mu$m no longer traces PAH emission at their redshifts; HLS18, because its large lensing magnification (54×) is not well constrained due to nearby objects (Rex et al. 2010). Otherwise, the lensing magnifications in the final HLS sample of 16 galaxies are small (median 1.1×). These galaxies are shown as stars in Figure 3.

In addition to the HLS galaxies, we have tested the indicator on individual 24 $\mu$m-bright lensed star-forming galaxies at $1.0 < z < 2.7$ for which we obtained near and mid-IR spectroscopic observations with the Large Binocular Telescope and *Spitzer*, and far-IR/sub-mm observations from the literature (Rujopakarn et al. 2012). The sample of five galaxies (A2218b, A2218a, A1835a, cB 58, and the Clone) is unique in that four members are of LIRG luminosity. The gravitational lensing gives us access to objects as low as $1.1 \times 10^{11}\ L_\odot$ (at a $z$ of 2.7). Although small, this sample thus provides an important verification of the accuracy of our method for typical star-forming galaxies at $z > 2$. Rujopakarn et al. (2012) find that the 24 $\mu$m indicator from this work estimates $L$(TIR) in good agreement with their far-IR $L$(TIR) values, with an average difference of 0.06 dex (although there is one outlier whose difference is 0.18 dex).

#### *4.1.4. Summary of the $L$(TIR) Indicator Tests with Individual Galaxies*

We have found from the tests using the ECDFS, HDFN, and lensed galaxies data that the systematic mid-IR excess issue discussed in the Introduction is virtually removed. Figure 5 uses the ECDFS sample to illustrate the extent of the mid-IR excess when templates for local galaxies are applied directly to high-$z$ galaxies, as is the case in the formulae given by Rieke et al. (2009). The results from the improved bolometric corrections are shown in comparison, which indicate that the overestimation problem is no longer present.

By using the new indicator, the resulting single-band 24 $\mu$m-derived $L$(TIR) has an average agreement with the far-IR observations of 0.02 dex in ECDFS (0.03 dex in HDFN) and a 1$\sigma$ scatter of 0.12 dex in the ECDFS, shown in Figure 3 (0.13 dex in the HDFN, shown in Figure 4). The 0.12–0.13 dex scatters are consistent with the 0.13 dex scatter of the relationship between $L$(24 $\mu$m) and $L$(TIR) in the local sample found by Rieke et al. (2009). The core distribution of luminosity difference between $L$(TIR) estimates from *Herschel* and the new indicator can be fitted by a Gaussian that has a $\sigma$ of 0.06 and 0.09 dex in ECDFS and HDFN, respectively, reflecting the degree of agreement where the extended structure assumption leads to a successful prediction of SED features. We found 8% of the ECDFS and HLS galaxies (9% of the HDFN galaxies) to have $L$(TIR) estimates from this method disagreeing by more than 0.2 dex from those of *Herschel*, with 2% and 6% on the over- and underestimation sides, respectively (2% and 7%, respectively, in the HDFN). Upon inspecting the individual SED fits, we determined that the overestimation is due to enhanced flux at 24 $\mu$m compared to star-forming galaxy SEDs, suggesting a mid-IR emission contribution from unidentified AGNs. SED fits for the 6% of objects in ECDFS (7% in HDFN) where the indicator underestimates $L$(TIR), indicates warmer far-IR SEDs than that predicted by the indicator, which suggests that their starburst structures are more compact, similar to local U/LIRGs, and inconsistent with our extended structure assumption. This is illustrated by lines (color-coded by $z$) in Figures 3, 4, and 5 that show where the compact U/LIRGs would lie if they are assumed (incorrectly) to have extended structure. Figures 3 and 4 indicate that, although some U/LIRGs at high $z$ could be compact, these are in the minority at a 10% level, which suggests that our assumption that high-$z$ star-forming galaxies indeed have extended star formation (that they are dominated by main-sequence star formation) is consistent with the properties of individual galaxies tested here.

We note that the fraction of compact objects here should be taken as an upper limit because far-IR selection of galaxies, such as presented, especially at $z > 2$, could be biased toward objects with warmer thermal dust emission and may cause compact objects to be overrepresented.

### 4.2. Tests of the 24 $\mu$m $L$(TIR) Indicator on Average SEDs

Next, we investigate the applicability of the new indicator on large galaxy survey samples using stacked photometry to represent the average properties of galaxies. We employ two samples for these tests: (1) the stacked 70 $\mu$m and 160 $\mu$m photometry of a 24 $\mu$m-selected sample from Lee et al. (2010) in COSMOS; and (2) the stacked 24 $\mu$m, 70 $\mu$m, 160 $\mu$m, 1.4 GHz, and 610 MHz observations of an NIR-selected sample from the ECDFS (Bourne et al. 2011). Unlike the earlier ECDFS, HDFN, and HLS samples, these $L$(TIR) estimates rely to a greater extent on extrapolating a fitted-SED to the dust emission peak. The goal of this section is thus not to determine the scatter for individual galaxies, but to test the indicator on a large sample across broad ranges of $z$ and $L$(TIR).

The Lee et al. (2010) sample stacks 70 $\mu$m and 160 $\mu$m observations of galaxies selected at 24 $\mu$m in COSMOS and represents the average SED properties of over 35000 galaxies. The stacks were done in bins of 24 $\mu$m flux ($0.06 < f_{24} < 3.00$ mJy) and redshift ($0 < z < 3$). Lee et al. then fit SEDs to the average 24 $\mu$m, 70 $\mu$m and 160 $\mu$m fluxes in each stacked bin to estimate $L$(TIR). We have excluded bins where the fraction of X-ray sources (i.e., AGN) exceeds 10% based on their Figure 3. For the actual $L$(TIR) calculation we use the average value of 24 $\mu$m flux and redshift in each bin (N. Lee 2011, private communication) to calculate the average $L$(TIR) of the bin, which can be compared with the estimates from Lee et al. (2010).

The Bourne et al. (2011) stacked sample of 3172 galaxies was selected using *Spitzer*/IRAC 3.6 $\mu$m and 4.5 $\mu$m photometry (i.e., a stellar mass selected sample) in the ECDFS. The selection in the near-IR provides an independent sample that has a potential to reveal selection effects (if any) inherent to mid- and far-IR selections (e.g., the Lee et al. 2010 and Kartaltepe et al. 2010 samples). Bourne et al. stacked observations of the sample in 7 redshift bins from $0 < z < 2.0$. These observations include 24 $\mu$m, 70 $\mu$m, 160 $\mu$m, 1.4 GHz and 610 MHz; the stacked fluxes of the *Spitzer*/MIPS bands were then used to fit a M51 SED to estimate $L$(TIR).

We compare with Lee et al. (2010) and Bourne et al. (2011) for our indicator and for the R09 and CE01 SED libraries separately in the left and right panels of Figure 6, respectively. A difference between the two panels is that the mid-IR excess becomes a problem for the R09 library well below $z = 1$ while it only becomes noticeable for CE01 templates at $z > 1.5$ (see also, Elbaz et al. 2010, Figure 1), as is observed in Figure 3. This is because the omission of silicate absorption features in the CE01 SED templates results in an overestimation of PAH-region flux in the local SED templates that coincidentally helps compensate for the evolution of PAH strength and delays the emergence of the mid-IR excess problem until beyond $z \sim 1.5$. The R09 templates correctly include the silicate absorption locally, and hence suffer a larger overestimation of $L$(TIR). We have now shown that the R09 templates can be used to describe the SEDs of galaxies and have estimated the bolometric corrections out to $z \sim 2.8$ given an appropriate choice of SED template based on the $\Sigma_{L(\mathrm{TIR})}$.

### 4.3. Verifying the Uncertainty Estimate for Individual Galaxies with an Independent Sample

Having established in Section 4.1 that the scatter of the $L$(TIR) estimates from our indicator is roughly 0.12–0.13 dex compared to far-IR $L$(TIR) measurements based on the ECDFS, HDFN, and HLS data, we now seek to verify this scatter estimate using a larger sample selected at a different wavelength.

We compare the new $L$(TIR) indicator to the $L$(TIR) estimates from the 70 $\mu$m-selected COSMOS sample (Kartaltepe et al. 2010). The entire sample contains 1503 galaxies at $0 < z < 3.5$ (median $z = 0.5$) with $L$(TIR) estimated by fitting IR photometry from *Spitzer* at the 8, 24, 70, and 160 $\mu$m bands to a collection of SED libraries, with the best fit selected via $\chi^2$ minimization among the Chary & Elbaz (2001), Dale & Helou (2002), Lagache et al. (2003), and Siebenmorgen & Krügel (2007) templates. For our comparison, we exclude sources with X-ray luminosity $>10^{42}$ erg s$^{-1}$ and those with radio excess. The sample is complete at 70 $\mu$m, by definition, and also at 24 $\mu$m, which allows the 70 and 24 $\mu$m color to be used as a criterion to select AGN that dominate the mid-IR emission. Specifically, we exclude objects with $\log(f_{70}/f_{24}) < 0.2z + 0.7$ (i.e., objects with enhanced 24 $\mu$m flux for a given 70 $\mu$m flux compared to the SEDs of star-forming galaxies), which removes 86 galaxies. Above $10^{12.5}$ $L_\odot$, the Kartaltepe et al. (2010) sample contains very few sources that do not harbor an AGN or a QSO. We limit our comparison sample to those with uncertainties in SED-fitted $L$(TIR) $< 0.35$ dex to avoid comparing to objects with uncertain luminosity.

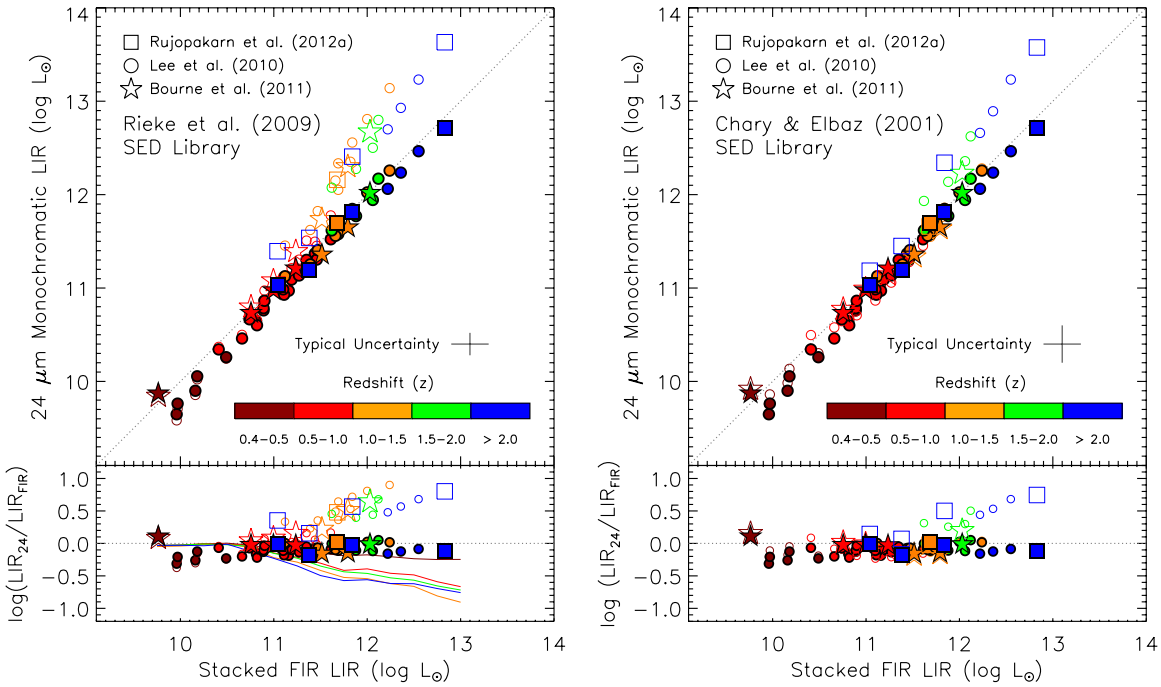


**Figure 6.** Comparison of $L$(TIR) from our single-band 24 $\mu$m indicator to $L$(TIR) measured from stacked and gravitationally lensed galaxies with far-IR observations. The comparison samples are from Lee et al. (2010) who determined $L$(TIR) at $0 < z < 3$ by stacking 70 $\mu$m and 160 $\mu$m observations of over 35,000 COSMOS galaxies (selected at 24 $\mu$m); from Bourne et al. (2011) whose $L$(TIR) was determined from stacking a broad range of observation from 24 $\mu$m to 610 MHz of 3,172 galaxies at $0 < z < 2$ in the ECDFS-FIDEL sample (selected at 3.6 and 4.5 $\mu$m); and from Rujopakarn et al. (2012) whose sample consists of gravitationally lensed galaxies at $1.0 < z < 2.7$. In the left and right panels, we show $L$(TIR) estimates from the new indicator as filled symbols in comparison to $L$(TIR) estimates from the R09 and CE01 SED library (open symbols in each panel). The lines in the bottom plot of the left panel illustrate the ratios that would result if the star-forming regions in high-$z$ IR galaxies were as compact as those found locally (see also, Figures 3). The right panel also illustrates our findings discussed in Section 4.2 that the mid-IR excess problem does not become apparent for the CE01 estimates until $z \sim 1.5$ because their overestimation of the PAH-region fluxes compared to local galaxies helps compensate the evolution of PAH strength at high $z$.

(A color version of this figure is available in the online journal.)

Among the 1503 galaxies selected at 70 $\mu$m, 463 are detected at 160 $\mu$m and their fluxes have been included in the SED fitting by Kartaltepe et al. (2010); 410 of these pass our AGN and uncertainty criteria. However, the 160 $\mu$m detections for these sources are of low significance: 236/410 galaxies (57%) are below 5$\sigma$ where the $\sigma$ value includes the confusion noise of 10 mJy for the survey (Frayer et al. 2009). Although a consistent $L$(TIR) is obtained if a stacked 160 $\mu$m flux is used for SED fitting, including these fluxes in the individual fits results in values typically high by 0.2 dex (Kartaltepe et al. 2010). This problem is consistent with Hogg & Turner (1998), who show that detections below 4–5$\sigma$ are biased toward brighter fluxes than their true values; see their Figure 2; this effect is commonly known as the Eddington bias. We therefore exclude the 160 $\mu$m-detected objects.

After applying the cuts discussed at the beginning of this section, we have 751 sources left. These sources have redshifts ranging from $z = 0.07$ to 1.81 with a mean and median redshift of 0.52 and 0.43. The luminosity of this subsample ranges from $L$(TIR) of $10^{9.5}$ to $10^{12.5}$ $L_\odot$ and the mean and median $L$(TIR)s are $10^{11.1}$ and $10^{11.2}$ $L_\odot$, respectively.

The comparison with $L$(TIR) estimated from the 24 $\mu$m fluxes alone indicates an average scatter of 0.25 dex relative to the assigned $L$(TIR) values. Some fraction of this scatter must arise in the assignment of $L$(TIR) by Kartaltepe et al. (2010); the median luminosity uncertainty within their work is 0.23 dex. That is, the 24 $\mu$m-only calculation agrees with their multi-wavelength fits virtually within the internal scatter of these fits. We quantify the contribution of uncertainties intrinsic to the new indicator in this test by conducting a Monte Carlo experiment to determine the scatter that must arise from our estimation of Kartaltepe et al. (2010) luminosities. We simulate a sample ($n = 10^4$) with a scatter of 0.23 dex and re-measure the values, introducing measurement errors in the process, which shows that an uncertainty of ~0.1 dex associated with the new indicator will broaden the intrinsic scatter of the Kartaltepe et al. (2010) sample to the 0.25 dex measured. This result is consistent with the 0.12–0.13 dex scatter found in Section 4.1.

### 4.4. Summary of the Tests

We tested the new 24 $\mu$m indicator on far-IR $L$(TIR) measurements of seven samples of galaxies selected with various techniques. These include (1) 91 galaxies in ECDFS selected at 250–500 $\mu$m; (2) 200 galaxies in HDFN selected at 100–500 $\mu$m; (3) 751 galaxies in COSMOS selected at 70 $\mu$m (Kartaltepe et al. 2010); (4) 16 far-IR-bright galaxies from Rex et al. (2010); (5) five 24 $\mu$m-bright lensed galaxies from Rujopakarn et al. (2012); (6) stacked photometry of 35,000 galaxies in COSMOS selected at 24 $\mu$m from Lee et al. (2010); (7) stacked photometry of 3172 galaxies in the ECDFS selected at 3.6 and 4.5 $\mu$m.

All of these tests indicate that the new indicator has eliminated the systematic overestimation of $L$(TIR) due to mismatching of SED templates, which is caused by the misassignment of the SEDs of compact local U/LIRGs to the extended U/LIRGs at high $z$ at the same $L$(TIR). For star-forming galaxies at $0.0 < z < 2.8$, the new indicator yields $L$(TIR) estimates consistent with *Herschel* far-IR measurements with an average agreement of 0.02–0.03 dex and a $1-\sigma$ scatter of 0.12–0.13 dex.

**Table 3**
The Luminosity of the Appropriate Rieke et al. (2009) SED Template to Describe SED of a Star-Forming Galaxy for a Given 24 $\mu$m Flux and Redshift

| $f_{24}$ | Redshift ($z$) | | | | | | | | | |
|---|---|---|---|---|---|---|---|---|---|---|
| (mJy) | 0.10 | 0.50 | 0.75 | 1.00 | 1.25 | 1.50 | 1.75 | 2.00 | 2.50 | 2.80 |
| 0.02 | ... | 9.9 | 10.1 | 10.2 | 10.4 | 10.5 | 10.5 | 10.5 | 10.6 | 10.8 |
| 0.05 | ... | 10.1 | 10.3 | 10.4 | 10.6 | 10.7 | 10.7 | 10.7 | 10.8 | 11.0 |
| 0.1 | ... | 10.3 | 10.5 | 10.6 | 10.8 | 10.9 | 10.8 | 10.8 | 11.0 | 11.1 |
| 0.2 | ... | 10.4 | 10.6 | 10.7 | 10.9 | 11.0 | 11.0 | 11.0 | 11.1 | 11.2 |
| 0.4 | 9.7 | 10.6 | 10.8 | 10.9 | 11.1 | 11.1 | 11.1 | 11.1 | 11.3 | 11.4 |
| 0.8 | 9.9 | 10.7 | 10.9 | 11.0 | 11.2 | 11.3 | 11.2 | 11.2 | 11.4 | 11.5 |
| 1.5 | 10.0 | 10.9 | 11.0 | 11.1 | 11.3 | 11.4 | 11.3 | 11.3 | 11.5 | 11.6 |
| 3.0 | 10.2 | 11.0 | 11.1 | 11.3 | 11.4 | 11.5 | 11.4 | 11.5 | 11.6 | 11.7 |

**Notes.** Dots indicate that the combination of flux and redshift would yield a SED template that is outside the luminosity range of the Rieke et al. (2009) SED library, $L(\mathrm{TIR}) = 10^{9.75}$–$10^{13}\,L_\odot$. As a reference, the $\log(L(\mathrm{TIR})/L_\odot)$ values for the archetypal local IR galaxies M82 and Arp 220 are 10.77 and 12.21, respectively.

Based on the samples in ECDFS and HDFN, we estimate the fraction of compact merger-triggered U/LIRGs beyond the local universe to be ∼10% (more discussion in Section 6.2).

We tabulate the luminosities of the recommended R09 SED templates to describe star-forming galaxies given their observed 24 $\mu$m fluxes and redshifts in Table 3. Even at the bright end of the flux range at high-$z$ (e.g., $f_{24} = 3.0$ mJy at $z = 2.8$, which corresponds to $L(\mathrm{TIR})$ of $2 \times 10^{14}\,L_\odot$), the appropriate R09 templates are those of local LIRGs with $L(\mathrm{TIR})$ of no more than $5 \times 10^{11}\,L_\odot$. In fact, it is evident from the table that most IR-luminous star-forming galaxies at $0 < z < 2.8$ exhibit spectral characteristics of local galaxies with $L(\mathrm{TIR})$ in the range of $10^{10}$–$3 \times 10^{11}\,L_\odot$.

## 5. $L$(TIR) −SFR RELATION

Finally, SFRs can be determined by making use of the relationship between $L(\mathrm{TIR})$ and the rest-frame $L(24\,\mu\mathrm{m})$, and subsequently the rest-frame $L(24\,\mu\mathrm{m})$ and SFR, originally given by Rieke et al. (2009). The introduction of the stretching factor, which effectively re-normalizes the SED templates, requires a modification of the relationship between $L(\mathrm{TIR})$ and $L(24\,\mu\mathrm{m})$. The original fit as given in Equation (A6) of Rieke et al. (2009) is

$$\log L(\mathrm{TIR})_{z=0} = 1.445 + 0.945 \log L(24\,\mu\mathrm{m},\ L_\odot). \quad (6)$$

The modified relationship is obtained by re-fitting Equation (6) with the stretching factor, $S_i$, multiplying both $L(\mathrm{TIR})$ and $L(24\,\mu\mathrm{m})$ for each template $i$. The re-fitted relation allows $L(24\,\mu\mathrm{m})$ to be calculated by substituting $L(\mathrm{TIR})_{\mathrm{new}}$ (from Equation (5)) in the following:

$$\log L(24\,\mu\mathrm{m}, L_\odot) = \frac{1}{0.982}[\log L(\mathrm{TIR})_{\mathrm{new}} - 1.096]. \quad (7)$$

To determine the SFR from the rest-frame $L(24\,\mu\mathrm{m})$, the calibration given by Rieke et al. (2009) remains valid. However, that calibration has a term that corrects for a decrease in $L(24\,\mu\mathrm{m})/L(\mathrm{TIR})$ ratio above $L(\mathrm{TIR}) = 10^{11} L_\odot$. Since the correction is motivated by an increase of the optical depth at high $L(\mathrm{TIR})$, which prevents the mid-IR emission from escaping, the threshold at which optical depth becomes significant depends directly on the geometry of the galaxy. In the same way that the extended structure of the galaxy beyond the local universe affects the IR-emitting environment, the optical depth will consequently be lower for a given $L(\mathrm{TIR})$ and the luminosity threshold where the optical depth should apply has to be scaled up by a stretching factor as well. The $S_i$ corresponding to the original threshold is 12.6× (referring to Table 1), yielding an IR luminosity threshold of $1.3 \times 10^{12}\,L_\odot$, which is equivalent to $L(24\,\mu\mathrm{m})$ of $1.6 \times 10^{11} L_\odot$. Therefore the relationship between SFR and $L(24\,\mu\mathrm{m})$ (from Equation (7)) is given by

$$\mathrm{SFR}(M_\odot\ \mathrm{yr}^{-1}) = 7.8 \times 10^{-10}\ L(24\,\mu\mathrm{m},\ L_\odot)$$

for $5 \times 10^9\,L_\odot \leqslant L(\mathrm{TIR}) \leqslant 1.3 \times 10^{12}\,L_\odot$ or $6 \times 10^8\,L_\odot \leqslant L(24\,\mu\mathrm{m}) \leqslant 1.6 \times 10^{11}\,L_\odot$. For $L(\mathrm{TIR}) > 1.3 \times 10^{12} L_\odot$ or $L(24\,\mu\mathrm{m}) > 1.6 \times 10^{11}\,L_\odot$,

$$\mathrm{SFR}(M_\odot\ \mathrm{yr}^{-1}) = 7.8 \times 10^{-10}\ L(24\,\mu\mathrm{m},\ L_\odot) \times [6.2 \times 10^{-12}\ L(24\,\mu\mathrm{m},\ L_\odot)]^{0.048} \quad (8)$$

This calibration is based on that of Kennicutt (1998) but with the Kroupa (2002) initial mass function, which yields SFRs a factor of 0.66 of those assuming the Salpeter (1955) initial mass function.

To summarize, the recipe to estimate $L(\mathrm{TIR})$ and SFR from a given set of 24 $\mu$m flux and redshift measurements is following. An IDL implementation of the steps below is available at our Web site.[4]

1. Check that the galaxy of interest does not harbor luminous AGN that dominates its 24 $\mu$m emission using the mid-IR (e.g., Donley et al. 2012) or X-ray criteria (e.g., by requiring $L_{\mathrm{X}}[0.5\text{–}8.0\,\mathrm{keV}] < 10^{42}$ erg s$^{-1}$).
2. To calculate total IR luminosity, interpolate for the coefficients $A'(z)$ and $B'(z)$ from Table 2 and calculate the luminosity distance for the object's redshift, then substitute these values in Equation (5) along with the observed 24 $\mu$m flux in mJy. The resulting $L(\mathrm{TIR})_{\mathrm{new}}$ is in unit of $L_\odot$.
3. To calculate SFR (in $\mathcal{M}_\odot$ yr$^{-1}$), first calculate the rest-frame $L(24\,\mu\mathrm{m})$ in $L_\odot$ using Equation (7), then substitute it in Equation (8) at the appropriate luminosity range.

## 6. DISCUSSION

In Section 6.1, we discuss the validity of using 24 $\mu$m observation at $0 < z < 2.8$ to estimate $L(\mathrm{TIR})$ and SFR; in Section 6.2, we discuss the implications of the $L(\mathrm{TIR})$ indicator in light of the test results from Section 4. In addition, we will discuss the implications of the new indicator on the maximum typical $L(\mathrm{TIR})$ for high-$z$ ULIRGs in Section 6.3.

### *6.1. Validity of the Aromatic Emission as an $L$(TIR) and SFR Indicator*

The success of the new indicator, which utilizes the luminosity at rest-frame wavelengths of 24 $\mu$m to 6 $\mu$m at $z = 0$ to 2.8, indicates that photometry dominated by aromatic emission is a surprisingly good tracer for $L(\mathrm{TIR})$. We discuss this result in terms of two major factors affecting the aromatic feature strength: the metallicity dependence and the presence of AGN.

The correlation of the aromatic luminosity to $L(\mathrm{TIR})$ was studied by Rigopoulou et al. (1999), Roussel et al. (2001) and Elbaz et al. (2002) using *ISO*; later by Wu et al. (2005) with *Spitzer*; and recently by Elbaz et al. (2011) with *Herschel*.

[4] http://ircamera.as.arizona.edu/rujopakarn2013

**Table 4**
Local Galaxies with $\Sigma_{L(\mathrm{TIR})}$ Measurement

| ID | *IRAS* ID | Distance[a] (Mpc) | Diameter (kpc) | $L$(TIR)[a] log($L_\odot$) | $\Sigma_{L(\mathrm{TIR})}$ log($L_\odot$ kpc$^{-2}$) | $\sigma\Sigma_L$ | Ref.[b] |
|---|---|---|---|---|---|---|---|
| NGC 2976 | F09431+6809 | 3.8 | 1.5 | 8.61 | 8.36 | 0.11 | 1 |
| NGC 4826 | F12542+2157 | 6.0 | 1.2 | 9.14 | 9.09 | 0.11 | 1 |
| NGC 2403 | F07320+6543 | 3.8 | 3.0 | 9.25 | 8.40 | 0.11 | 1 |
| NGC 925 | F02242+3321 | 9.8 | 6.1 | 9.46 | 7.99 | 0.11 | 1 |
| NGC 1512 | ... | 11.3 | 3.2 | 9.49 | 8.58 | 0.11 | 1 |
| NGC 5866 | F15051+5557 | 13.0 | 1.8 | 9.51 | 9.10 | 0.11 | 1 |
| NGC 2841 | ... | 10.5 | 4.9 | 9.52 | 8.24 | 0.11 | 1 |
| NGC 4559 | F12334+2814 | 11.9 | 5.0 | 9.62 | 8.33 | 0.11 | 1 |
| NGC 4736 | 12485+4123 | 5.7 | 1.7 | 9.79 | 9.43 | 0.11 | 1 |
| NGC 3198 | F10168+4547 | 14.7 | 3.8 | 9.81 | 8.76 | 0.11 | 1 |
| NGC 3184 | 10152+4140 | 11.9 | 6.5 | 9.86 | 8.34 | 0.11 | 1 |
| NGC 3351 | F10413+1157 | 10.8 | 2.2 | 9.89 | 9.31 | 0.11 | 1 |
| NGC 3938 | F11502+4423 | 13.1 | 4.7 | 9.99 | 8.75 | 0.11 | 1 |
| NGC 4569 | F12343+1326 | 17.8 | 3.1 | 10.08 | 9.20 | 0.11 | 1 |
| NGC 5055 | F13135+4217 | 8.4 | 4.3 | 10.15 | 8.99 | 0.11 | 1 |
| NGC 5033 | F13111+3651 | 14.7 | 1.1 | 10.19 | 10.21 | 0.11 | 1 |
| NGC 3627 | F11176+1315 | 9.3 | 3.5 | 10.44 | 9.46 | 0.11 | 1 |
| NGC 5194 | F13277+4727 | 8.8 | 5.7 | 10.48 | 9.07 | 0.11 | 1 |
| NGC 7331 | F22347+3409 | 16.2 | 4.7 | 10.64 | 9.40 | 0.11 | 1 |
| NGC 23 | F00073+2538 | 63.9 | 1.2 | 11.11 | 11.06 | 0.11 | 2 |
| NGC 6701 | F18425+6036 | 60.6 | 0.7 | 11.11 | 11.52 | 0.11 | 2 |
| UGC1845 | F02208+4744 | 66.4 | 0.8 | 11.13 | 11.42 | 0.11 | 2 |
| NGC 5936 | F15276+1309 | 65.1 | 0.6 | 11.13 | 11.74 | 0.11 | 2 |
| MCG+02-20-003 | F07329+1149 | 72.4 | 0.8 | 11.14 | 11.46 | 0.11 | 2 |
| NGC 2369 | F07160-6215 | 47.1 | 0.8 | 11.16 | 11.44 | 0.11 | 2 |
| ESO320-G030 | F11506-3851 | 40.4 | 0.9 | 11.16 | 11.35 | 0.11 | 2 |
| IC5179 | F22132-3705 | 50.0 | 1.6 | 11.22 | 10.92 | 0.11 | 2 |
| NGC 2388 | F07256+3355 | 61.9 | 0.8 | 11.29 | 11.55 | 0.11 | 2 |
| NGC 7771 | F23488+1949 | 61.2 | 1.0 | 11.40 | 11.47 | 0.11 | 2 |
| MCG+12-02-001 | F00506+7248 | 68.9 | 0.8 | 11.50 | 11.80 | 0.11 | 2 |
| ... | F03359+1523 | 146.9 | 0.1 | 11.53 | 13.94 | 0.17 | 3 |
| NGC 1614 | F04315-0840 | 67.1 | 0.9 | 11.66 | 11.87 | 0.11 | 4 |
| UGC2369 | F02512+1446 | 130.7 | 0.1 | 11.66 | 13.96 | 0.16 | 3 |
| Arp236 | F01053-1746 | 84.2 | 2.6 | 11.71 | 10.98 | 0.11 | 4 |
| Arp193 | F13182+3424 | 107.1 | 0.8 | 11.73 | 12.03 | 0.11 | 4 |
| UGC4881 | F09126+4432 | 172.7 | 0.1 | 11.75 | 13.56 | 0.12 | 3 |
| Arp299 | F11257+5850 | 51.2 | 0.4 | 11.94 | 12.80 | 0.11 | 4 |
| ... | F17132+5313 | 218.9 | 0.1 | 11.95 | 13.76 | 0.15 | 3 |
| ... | F15163+4255 | 180.8 | 0.2 | 11.95 | 13.29 | 0.11 | 3 |
| ... | F10565+2448 | 188.9 | 0.8 | 11.99 | 12.29 | 0.11 | 4 |
| VIIZw31 | F05081+7936 | 230.2 | 2.1 | 12.00 | 11.46 | 0.11 | 5 |
| ... | F23365+3604 | 269.8 | 1.1 | 12.19 | 12.21 | 0.11 | 5 |
| Arp220 | F15327+2340 | 85.6 | 0.2 | 12.27 | 13.77 | 0.11 | 6 |
| ... | F17207-0014 | 188.2 | 0.9 | 12.45 | 12.65 | 0.10 | 4 |

**Notes.** Reproduced from Table 2 of Rujopakarn et al. (2011). Uncertainties in $L$(TIR) estimates are dominated by distance measurement uncertainties, which are not published in the Sanders et al. (2003) catalog; we use error bars of 0.1 dex for $L$(TIR)–$\Sigma_{L(\mathrm{TIR})}$ parameterizations fitting and to estimate the $\sigma\Sigma_L$.

[a] Distance and $L$(TIR) from Sanders et al. (2003) and adjust to match our cosmology.

[b] Diameters references 1. measured from *Spitzer*/MIPS 24 $\mu$m imaging taken by SINGS (e.g., Calzetti et al. 2007), 2. measured from *Hubble*/NICMOS Pa-$\alpha$ taken by Alonso-Herrero et al. (2006), 3. 8.4 GHz radio sizes given by Condon et al. (1991), 4. CO (3–2) sizes given by Iono et al. (2009), 5. CO (2–1) or CO (1–0) sizes given by Downes & Solomon (1998), 6. 5 GHz radio size based on Rovilos et al. (2003).

Although large scatter in $L(8\ \mu\mathrm{m})/L(\mathrm{TIR})$ is apparent over a large range of metallicity (Calzetti et al. 2007), for high-metallicity systems ($Z > 1/3\,Z_\odot$, which is equivalent to $12 + \log(\mathrm{O/H}) \gtrsim 8.2$), Calzetti (2010) reports that the stellar-continuum-subtracted PAH emission shows a good correlation with the SFR. Furthermore, Engelbracht et al. (2008) and Smith et al. (2007) find that the ratio of aromatic luminosity to $L$(TIR) does not vary significantly at metallicity $\gtrsim 1/3\,Z_\odot$. Galaxies at $z \sim 2$ have on average 0.3 dex lower metallicity than local galaxies (Erb et al. 2006). Therefore, galaxies more massive than $3 \times 10^9\ M_\odot$ should be sufficiently metal rich ($>1/3\,Z_\odot$) that the $L$(TIR)/PAH calibration is valid. If we consider the ratio of aromatic-luminosity-to-$L$(TIR) as a function of metallicity in the left panel of Figure 7 within the range of metallicity expected at high-$z$, the scatter of the relationship between aromatic luminosity and $L$(TIR) is in fact about 0.1 dex in the non-Seyfert/LINER sample. This suggests aromatic luminosity to be a good indicator for $L$(TIR) at high-$z$ given that an effort is made to exclude AGNs from the sample (such as the AGN exclusion criteria employed in tests in Sections 4.1 and 4.2).

**Table 5**
High-$z$ Galaxies with $\Sigma_{L(\mathrm{TIR})}$ Measurement

| ID | $z$ | Diameter (kpc) | $L(\mathrm{TIR})_{\mathrm{old}}$ log($L_\odot$) | $\sigma L$ | $\Sigma_{L(\mathrm{TIR})}$ log($L_\odot$ kpc$^{-2}$) | $\sigma\Sigma_L$ | Ref.[a] |
|---|---|---|---|---|---|---|---|
| RGJ105146.61+572033.4 | 2.383 | 4.2 | 13.37 | 0.135 | 12.23 | 0.247 | 3 |
| SMMJ105151.69+572636.1 | 1.147 | 6.1 | 12.60 | 0.139 | 11.14 | 0.209 | 4, 5 |
| RGJ105154.19+572414.6 | 0.922 | 4.0 | 12.21 | 0.132 | 11.11 | 0.253 | 3 |
| SMMJ105155.47+572312.8 | 2.686 | 2.2 | 13.13 | 0.157 | 12.55 | 0.372 | 4, 5 |
| SMMJ105158.02+571800.3 | 2.239 | 6.7 | 13.21 | 0.146 | 11.67 | 0.203 | 4, 5 |
| RGJ105159.90+571802.4 | 1.047 | 5.4 | 12.83 | 0.132 | 11.47 | 0.213 | 3 |
| SMMJ105201.25+572445.8 | 2.148 | 3.3 | 12.90 | 0.138 | 11.97 | 0.295 | 4, 5 |
| J123607+621328 | 0.435 | 5.3 | 10.84 | 0.131 | 9.50 | 0.164 | 6, 7, 8 |
| J123615+620946 | 1.263 | 5.2 | 12.16 | 0.133 | 10.84 | 0.194 | 6, 7, 8 |
| SMMJ123616.15+621513.7 | 2.578 | 8.0 | 13.72 | 0.131 | 12.02 | 0.176 | 2, 6, 7, 8 |
| J123617+621011 | 0.845 | 3.6 | 11.05 | 0.135 | 10.04 | 0.229 | 6, 7, 8 |
| J123618+621550 | 1.870 | 2.6 | 12.96 | 0.131 | 12.24 | 0.181 | 6, 7, 8 |
| J123619+621252 | 0.473 | 1.8 | 11.62 | 0.130 | 11.22 | 0.183 | 6, 7, 8 |
| SMMJ123622.65+621629.7 | 2.466 | 9.7 | 13.72 | 0.130 | 11.85 | 0.160 | 2, 6, 7, 8 |
| SMMJ123629.13+621045.8 | 1.013 | 6.6 | 12.71 | 0.130 | 11.18 | 0.143 | 1, 2, 6 |
| J123630+620923 | 0.953 | 3.7 | 11.80 | 0.131 | 10.77 | 0.223 | 6, 7, 8 |
| J123633+621005 | 1.016 | 7.5 | 12.58 | 0.130 | 10.94 | 0.165 | 6, 7, 8 |
| J123634+621213 | 0.456 | 5.4 | 11.72 | 0.130 | 10.36 | 0.144 | 6, 7, 8 |
| J123634+621241 | 1.219 | 6.4 | 13.08 | 0.130 | 11.58 | 0.138 | 6, 7, 8 |
| J123635+621424 | 2.011 | 1.9 | 14.03 | 0.130 | 13.58 | 0.195 | 6, 7, 8 |
| J123641+620948 | 0.518 | 2.9 | 11.33 | 0.130 | 10.51 | 0.173 | 6, 7, 8 |
| RGJ123645.89+620754.1 | 1.433 | 4.2 | 13.36 | 0.131 | 12.22 | 0.193 | 3, 6 |
| J123646+620833 | 0.971 | 4.9 | 12.76 | 0.130 | 11.49 | 0.192 | 6, 7, 8 |
| J123649+621313 | 0.475 | 4.6 | 11.14 | 0.131 | 9.92 | 0.179 | 6, 7, 8 |
| J123650+620801 | 0.559 | 3.5 | 11.09 | 0.131 | 10.11 | 0.213 | 6, 7, 8 |
| J123651+621030 | 0.410 | 5.1 | 11.44 | 0.130 | 10.13 | 0.165 | 6, 7, 8 |
| RGJ123653.37+621139.6 | 1.275 | 5.8 | 13.02 | 0.131 | 11.60 | 0.168 | 3, 6 |
| J123655+620917 | 0.419 | 2.6 | 11.39 | 0.130 | 10.66 | 0.181 | 6, 7, 8 |
| J123655+620808 | 0.792 | 4.1 | 12.22 | 0.130 | 11.09 | 0.167 | 6, 7, 8 |
| J123659+621449 | 0.761 | 5.7 | 11.84 | 0.130 | 10.43 | 0.174 | 6, 7, 8 |
| J123704+620755 | 1.253 | 6.5 | 13.26 | 0.131 | 11.74 | 0.174 | 6, 7, 8 |
| J123705+621153 | 0.902 | 9.1 | 12.31 | 0.130 | 10.49 | 0.152 | 6, 7, 8 |
| J123708+621056 | 0.422 | 3.0 | 11.26 | 0.130 | 10.42 | 0.211 | 6, 7, 8 |
| RGJ123710.60+622234.6 | 1.522 | 3.4 | 12.98 | 0.171 | 12.02 | 0.237 | 3 |
| SMMJ123711.98+621325.7 | 1.992 | 6.9 | 12.79 | 0.132 | 11.22 | 0.197 | 1, 2, 6 |
| J123713+621603 | 0.938 | 5.5 | 11.72 | 0.131 | 10.34 | 0.183 | 6, 7, 8 |
| J123714+621558 | 0.567 | 7.6 | 10.93 | 0.131 | 9.27 | 0.154 | 6, 8 |
| J123716+621643 | 0.557 | 4.5 | 11.51 | 0.130 | 10.31 | 0.187 | 6, 7, 8 |
| J123716+621007 | 0.411 | 3.0 | 11.18 | 0.130 | 10.33 | 0.211 | 6, 7, 8 |
| J123721+621346 | 1.019 | 4.4 | 11.97 | 0.131 | 10.79 | 0.210 | 6, 7, 8 |

**Notes.** Reproduced from Table 1 of Rujopakarn et al. (2011) with omission of objects whose diameters were measured with CO observations, which are excluded from the fit in Section 3.

[a] 1. Chapman et al. (2004), 2. Chapman et al. (2005), 3. Casey et al. (2009), 4. Biggs & Ivison (2008), 5. Ivison et al. (2007) 6. GOODS *Spitzer* Legacy Data, M. Dickinson et al., in preparation, 7. Muxlow et al. (2005), 8. Morrison et al. (2010).

Smith et al. (2007) found that AGNs can significantly suppress the PAH emission (see also, Moorwood 1986; Roche et al. 1991; Genzel et al. 1998). The suppression of PAH luminosity is shown in Figure 7 (left) using the total PAH luminosities measured by Smith et al. (2007) and a metallicity measurement from Moustakas et al. (2010). Moderate luminosity AGNs, however, do not affect the PAH emission of the entire host galaxy. Diamond-Stanic & Rieke (2010) use *Spitzer*/IRS to compare nuclear and non-nuclear spectra of nearby Seyfert galaxies and found that while the PAH features in the nuclear spectra are clearly suppressed, the features are of normal strength in the outer disk. Therefore, with regard to using PAH emission to trace $L$(TIR) in galaxies hosting moderate luminosity AGNs, the PAH suppression due to AGNs is likely limited to the nuclear region and PAH emission arising from the rest of the galaxy should still provide a good tracer of the SFR.

We further test the validity of aromatic emission (e.g., 8 $\mu$m rest-frame observation) as a measure of $L$(TIR) in a sample of H II-dominated galaxies with moderate to high metallicity in the right panel of Figure 7. In this figure, the 8 $\mu$m observations are from *Spitzer* and the $L$(TIR) estimates are based on the *IRAS* all-sky survey using 12, 25, 60, and 100 $\mu$m observations (Sanders et al. 2003). This sample is chosen such that it mimics the population of star-forming galaxies expected at high $z$: high-metallicity normal star-forming galaxies without AGNs. The scatter of the relationship between $L(8\,\mu\mathrm{m})$ and $L$(TIR) in Figure 7 is 0.14 dex with the ratio $L(\mathrm{TIR})/\mathrm{L}(8\,\mu\mathrm{m})$ of $4.3 \pm 1.6$. Elbaz et al. (2011) reports a similar $L(\mathrm{TIR})/\mathrm{L}(8\,\mu\mathrm{m})$ of $4.9^{+2.9}_{-2.2}$ for their GOODS-*Herschel* sample out to $z \sim 3$ (that is, a $1\sigma$ spread of $\sim$0.23 dex) without applying corrections for the shape of the SED (see also Nordon et al. 2012).

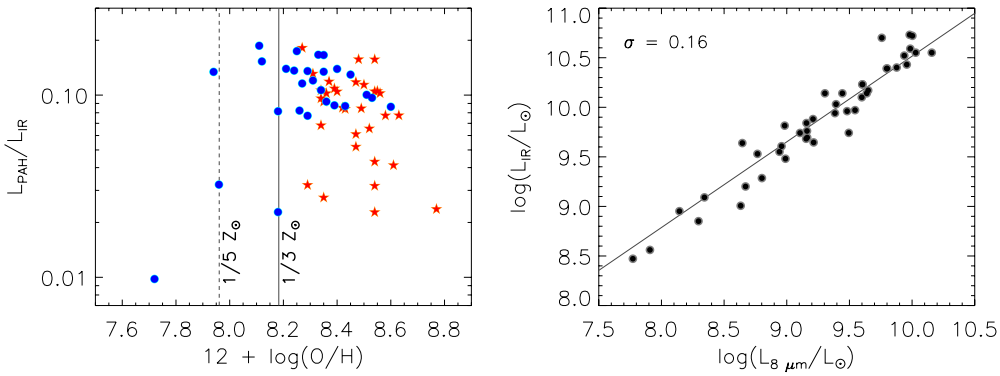


**Figure 7.** (Left) The sources of scatter in using aromatic emissions (e.g., PAH) to predict $L$(TIR) and SFR are primarily the metallicity dependence and the presence of AGNs. Blue dots and red stars show the ratios of aromatic luminosity to $L$(TIR) as a function of metallicity for H II- and AGN-dominated local galaxies, respectively (Smith et al. 2007). For H II-dominated galaxies with metallicity greater than $1/3\,Z_\odot$ (solid vertical line), which is similar to the environment of high-$z$ star-forming galaxies, the correlation of aromatic luminosity, $L_{\rm PAH}$, and $L$(TIR) has a ∼0.1 dex scatter, suggesting that aromatic emission could serve as a good $L$(TIR) and SFR indicators at high $z$. (Right) The correlation between the rest-frame $L(8\,\mu{\rm m})$ and $L$(TIR) for local star-forming galaxies that are dominated by H II-emission and have high metallicity, similar to those expected at high $z$, has a scatter of 0.14 dex. The small scatter underlines the potential of using aromatic emission as an $L$(TIR) and SFR indicator.

(A color version of this figure is available in the online journal.)

### *6.2. Modes of Star Formation and the Validity of the Main Sequence Assumption*

In the process of constructing our $L$(TIR) indicator, we have assumed that all non-local star-forming galaxies lie in the main-sequence. In other words, the new indicator assumes that star formation beyond the local universe is not dominated by compact, merger-induced, nuclear-concentrated starbursts. The results from Sections 4.1 and 4.2 indicate that this assumption is consistent with the nature of high-$z$ galaxies: (1) the potentially compact starbursts, whose $L$(TIR) values are underestimated compared to their far-IR $L$(TIR), comprise only 6%–7% of the sample, and (2) the comparison of stacked samples shows no systematic discrepancies.

At low redshifts ($z \lesssim 0.5$), the bottom panel of Figure 3 and the top panel of Figure 4 suggest that the $L$(TIR) values from the new indicator converge to within 0.25 dex with those from the Rieke et al. (2009) indicator, which use compact local starburst SED templates without the $\Sigma_{L({\rm TIR})}$ corrections, at all $L$(TIR) values up to $10^{13}\,L_\odot$. The agreement is better at lower $L$(TIR), e.g., ∼0.1 dex at $10^{12}\,L_\odot$, which is typical for star-forming U/LIRGs at low $z$. Thus, for practical purposes, both indicators can be used interchangeably below $z \sim 0.5$ regardless of the compactness of galaxies' star-forming regions.

At intermediate $z$ ($0.5 \lesssim z \lesssim 1$), the precise fractions of galaxies that form stars in the extended and compact modes remain a subject of controversy. Lotz et al. (2011) discuss the various merger indicators critically to remove the discrepancies as much as possible and find that mergers are, in fact, important out to $z \sim 1.5$, with minor mergers about three times more frequent than major ones. To first order, the dominance of minor rather than major mergers appears consistent with the tests in Section 4.2, which support our initial assumption that a majority of star-forming galaxies beyond the local universe reside in the main sequence of star-forming galaxies. The main sequence picture for IR galaxies is also advocated by Elbaz et al. (2011) who find that nearly 80% of IR star-forming galaxies studied by *Herschel* have the ratio of the $8\,\mu$m luminosity to $L$(TIR) consistent with being in the extended mode of star formation (the median redshift of their study varies with $L$(TIR), from $z_{\rm median} = 0.3$ for $10^{10}\,L_\odot$ to $z_{\rm median} = 1.5$ for $10^{12}\,L_\odot$; see their Figure 15). A remaining issue is the precise transition scheme from the merger-induced mode of star formation found locally to the extended mode of star formation at high $z$. This is actually among the fundamental questions in galaxy evolution because it is closely tied to the mechanism of the decline of SFR since $z \sim 1.5$. A theoretical interpretation was provided by Hopkins et al. (2010), but future observations will be required to study this transition definitively.

Avid readers will have noticed that most of the individual test galaxies at redshift $z = 0.5$–1 in Section 4.1 are less luminous than $10^{12}\,L_\odot$. The space density of ULIRGs at these redshifts is too sparse for a large number of them to be present in pencil-beam surveys, such as those used in Section 4.1. Therefore, while we have tested the new indicator thoroughly with typical star-forming galaxies at $z = 0.5$–1, the formalism may not be adequate to describe luminous ULIRGs in this redshift range. But ULIRGs at the bright-end of the luminosity function at $z < 1$, such as these, are often bright enough to be within reach of the current far-IR, sub-mm, and radio facilities to provide direct measurement of the $L$(TIR). The results from the new $24\,\mu$m indicator should therefore be cross-checked with these independent bands when possible.

We must also caution that there are very few galaxies with $L({\rm TIR}) > 10^{13}\,L_\odot$ in the seven tests in Section 4 due to their rarity, even at $z > 2.5$. This hyperluminous regime could be dominated by merger-triggered compact starbursts even at high $z$ (e.g., Hopkins et al. 2010), which will result in an underestimation of $L$(TIR) and SFR by up to 0.5 dex (refer to color-coded lines representing compact objects as a function of $z$ in Figures 3 and 4). For the same reasons that prevent us from thoroughly testing this luminosity regime, we expect compact hyperluminous starbursts to be rare, and will not affect the usefulness of the new indicator within the goal of providing a tracer of SFR in typical U/LIRGs (e.g., $L^*$ galaxies) out to $z \sim 2.8$, where most of the stellar mass in the universe was formed. Again, these most luminous galaxies will be bright enough for independent measurements of SFR using far-IR, sub-mm, and radio observations.

### *6.3. The Eddington Luminosity of ULIRGs*

It has been suggested that local ULIRGs are optically thick to mid-IR photons and radiation pressure may play a role in limiting their maximum luminosity (Thompson et al. 2005; Younger

et al. 2008; Thompson 2009). If the degree of compactness is assumed to be similar for both the local and high-$z$ ULIRGs, the IR emission of high-$z$ ULIRGs with $L$(TIR) commonly found far above their local counterparts might exceed the Eddington luminosity. Our results ease the concerns about the Eddington limit of ULIRGs at high $z$ for two reasons. First, galaxies at higher $L$(TIR) are affected by the mid-IR excess to a greater extent. The new indicator would therefore lower the $L$(TIR) estimates especially for high-luminosity galaxies. To test the effects of $L$(TIR) reduction to the luminosity functions of galaxies, we construct a set of IR LFs of 24 $\mu$m sources at $0 < z < 2.5$ using the 24 $\mu$m observations from COSMOS (e.g., Sanders et al. 2007) and find that the bright-ends of the LFs in all redshift bins are below $L$(TIR) of $\sim 10^{13}\ L_\odot$ (quantitatively, galaxies with $L$(TIR) above $10^{13}\ L_\odot$ are rarer than $10^{-6}$ Mpc$^{-3}$ dex$^{-1}$ in all redshift bins), which suggests that the maximum $L$(TIR) of star-forming galaxies is in general $\lesssim 10^{13}\ L_\odot$. Second, the success of the corrections for the size evolution described in Rujopakarn et al. (2011) as well as this work to account for the general IR SED evolution indicate that the great majority of high-$z$ IR galaxies are physically extended, which lowers the optical depth of the galaxy. Both the lower $L$(TIR) and optical depth imply that high-$z$ ULIRGs are emitting below the Eddington limit and that the maximum $L$(TIR) of these galaxies is not governed by radiation pressure.

## 7. CONCLUSIONS

The use of single-band mid-IR indicators (such as 24 $\mu$m observations) to estimate $L$(TIR) has previously been affected by the differences between the structure of local U/LIRGs, from which the SED templates were constructed, and those of the galaxies in the cosmological surveys being studied. Starbursts in the local U/LIRGs are interaction-induced and compact (sub-kpc), while U/LIRGs at high $z$ are typically much more extended ($\sim$few kpc), with surface areas $\sim$100 times larger than their local counterparts. The resulting larger surface area of the photodissociation regions harboring aromatic emission leads to stronger aromatic features at high $z$ that appears as an evolution in aromatic strength with $z$. The ultimate implication of this morphological difference is that single-band mid-IR observations, which at $z > 1$ probe the aromatic-dominated SED region, will overpredict $L$(TIR) and SFR compared to far-IR measurements if the relationship of local SED templates to $L$(TIR) is assumed for the calculation of the bolometric and k-corrections.

Following the Rujopakarn et al. (2011) result that $\Sigma_{L(\mathrm{TIR})}$ can serve as a good predictor for the appropriate SED of star-forming galaxies, we construct a new 24 $\mu$m single-band $L$(TIR) and SFR indicator for star-forming galaxies at redshift $0 < z < 2.8$. The resulting 0.03 dex average agreement (0.13 dex scatter) between $L$(TIR) estimates from the new single-band 24 $\mu$m indicator and those from multi-band far-IR SED fitting support the Rujopakarn et al. (2011) result that $\Sigma_{L(\mathrm{TIR})}$ is indeed the dominant factor affecting the SED shapes of star-forming galaxies.

For the purpose of estimating $L$(TIR) and SFR, we recommend using the new indicator at $0 < z < 2.8$. A step-by-step recipe is given in Section 5. The new indicator converges with that of Rieke et al. (2009) for local and low $z$ galaxies (Section 6.2). But unlike the Rieke et al. (2009) indicator, we provide a formalism that fits the extended, main sequence, star formation that is dominant at high $z$. Since the compact, nuclear form of starburst is uncommon beyond the local neighborhood (<10%; see Figures 3 and 4)), our formalism is appropriate in the great majority of cases. However, if an object is known a priori to be a compact starburst (e.g., from high-resolution optical or interferometric radio observations), we recommend readers to apply the bolometric correction factor given by Rieke et al. (2009) in their Equation (14). On the other hand, even where the structure of the star-forming region is not known a priori, we quote an overall scatter of 0.13 dex, when AGNs are identified and excluded from the sample using X-ray and 3.6–8.0 $\mu$m (i.e., *Spitzer*/IRAC) observations.

We thank Daniel Eisenstein for insightful discussions, and J. D. Smith for the $L_{\mathrm{PAH}}/L$(TIR) data. This work is supported by contract 1255094 from Caltech/JPL to the University of Arizona. W.R. gratefully acknowledges the support from the Thai Government Scholarship.

## APPENDIX

## MITIGATION OF POTENTIALLY BLENDED OBJECTS IN THE *HERSCHEL* OBSERVATIONS

Since the *Herschel*/PACS and SPIRE source extraction procedure is designed to yield a sample for the fiducial $L$(TIR) estimates to test the new indicator, an emphasis is given to achieving an unbiased sample, rather than maximizing the number of detectable sources. To this end, we develop a figure of merit (FoM) and criteria by which we exclude potentially blended objects. This is important to mitigate the cases of intervening objects contributing additional flux to the object of interest. The FoM is defined in an unbiased manner based on the 24 $\mu$m prior catalog by

$$\mathrm{FoM} = \sum_i [(R_i/4)^{-1}(d_i/6'')^{-1}] \tag{A1}$$

where $R_i$ is the ratio of the 24 $\mu$m flux of the prior object to the 24 $\mu$m fluxes of other nearby objects within the radius (9.″1) of SPIRE 250 $\mu$m beam from the prior and $d_i$ is the distance from the prior object to the corresponding nearby objects. The 250 $\mu$m beam is chosen for this criteria because it is the band at which most of our ECDFS and HDFN samples are detected. The normalizations for $R_i$ and $d_i$ are chosen such that the FoM increases rapidly if other sources that are expected to be in the beam could be in within the same SPIRE pixel (6″) or could have comparable SPIRE fluxes to the object at the prior position. The $R_i$ normalization value is determined by inspecting the variation of the ratios of 24 and 250 $\mu$m fluxes for SED templates in the Rieke et al. (2009) library, which gives a $\sim$4 times variation. That is, if the 24 $\mu$m flux of a nearby object is less than $\sim$1/4 that of the prior object, it is unlikely that its 250 $\mu$m flux will be comparable to the prior (and hence cause a blending problem) at redshift 0–2.8, assuming the Rieke et al. (2009) SED shape. We emphasize that the exclusion does not depend sensitively on the normalizations in the FoM, and we have adopted a conservative rejection threshold by excluding objects with FoM >5 from the final catalog, rejecting only the most likely blended objects.

## REFERENCES

Alonso-Herrero, A., Rieke, G. H., Rieke, M. J., et al. 2006, ApJ, 650, 835
Armus, L., Charmandaris, V., Bernard-Salas, J., et al. 2007, ApJ, 656, 148
Barro, G., Pérez-González, P. G., Gallego, J., et al. 2011, ApJS, 193, 30
Biggs, A. D., & Ivison, R. J. 2008, MNRAS, 385, 893
Bourne, N., Dunne, L., Ivison, R. J., et al. 2011, MNRAS, 410, 1155

Buat, V., Takeuchi, T. T., Iglesias-Páramo, J., et al. 2007, ApJS, 173, 404
Calzetti, D. 2010, arXiv:1010.4996
Calzetti, D., Kennicutt, R. C., Engelbracht, C. W., et al. 2007, ApJ, 666, 870
Calzetti, D., Wu, S.-Y., Hong, S., et al. 2010, ApJ, 714, 1256
Casey, C. M., Chapman, S. C., Beswick, R. J., et al. 2009, MNRAS, 399, 121
Chakrabarti, S., & McKee, C. F. 2005, ApJ, 631, 792
Chanial, P., Flores, H., Guiderdoni, B., et al. 2007, A&A, 462, 81
Chapman, S. C., Blain, A. W., Smail, I., & Ivison, R. J. 2005, ApJ, 622, 772
Chapman, S. C., Smail, I., Windhorst, R., Muxlow, T., & Ivison, R. J. 2004, ApJ, 611, 732
Chary, R., & Elbaz, D. 2001, ApJ, 556, 562
Chary, R.-R., & Pope, A. 2010, arXiv:1003.1731
Condon, J. J. 1974, ApJ, 188, 279
Condon, J. J., Huang, Z.-P., Yin, Q. F., & Thuan, T. X. 1991, ApJ, 378, 65
Cooper, M. C., Yan, R., Dickinson, M., et al. 2012, MNRAS, 425, 2116
Daddi, E., Elbaz, D., Walter, F., et al. 2010, ApJL, 714, L118
Dale, D. A., & Helou, G. 2002, ApJ, 576, 159
Damen, M., Labbé, I., van Dokkum, P. G., et al. 2011, ApJ, 727, 1
Diamond-Stanic, A. M., & Rieke, G. H. 2010, ApJ, 724, 140
Dole, H., Lagache, G., Puget, J.-L., et al. 2006, A&A, 451, 417
Dole, H., Rieke, G. H., Lagache, G., et al. 2004, ApJS, 154, 93
Donley, J. L., Koekemoer, A. M., Brusa, M., et al. 2012, ApJ, 748, 142
Downes, D., & Solomon, P. M. 1998, ApJ, 507, 615
Egami, E., Rex, M., Rawle, T. D., et al. 2010, A&A, 518, L12
Elbaz, D., Cesarsky, C. J., Chanial, P., et al. 2002, A&A, 384, 848
Elbaz, D., Dickinson, M., Hwang, H. S., et al. 2011, A&A, 533, A119
Elbaz, D., Hwang, H. S., Magnelli, B., et al. 2010, A&A, 518, L29
Engelbracht, C. W., Rieke, G. H., Gordon, K. D., et al. 2008, ApJ, 678, 804
Erb, D. K., Shapley, A. E., Pettini, M., et al. 2006, ApJ, 644, 813
Farrah, D., Lonsdale, C. J., Weedman, D. W., et al. 2008, ApJ, 677, 957
Frayer, D. T., Sanders, D. B., Surace, J. A., et al. 2009, AJ, 138, 1261
Genzel, R., Lutz, D., Sturm, E., et al. 1998, ApJ, 498, 579
Genzel, R., Tacconi, L. J., Gracia-Carpio, J., et al. 2010, MNRAS, 407, 2091
Hogg, D. W., & Turner, E. L. 1998, PASP, 110, 727
Hopkins, A. M., & Beacom, J. F. 2006, ApJ, 651, 142
Hopkins, P. F., Younger, J. D., Hayward, C. C., Narayanan, D., & Hernquist, L. 2010, MNRAS, 402, 1693
Iono, D., Wilson, C. D., Yun, M. S., et al. 2009, ApJ, 695, 1537
Ivison, R. J., Greve, T. R., Dunlop, J. S., et al. 2007, MNRAS, 380, 199
Johansson, D., Horellou, C., Sommer, M. W., et al. 2010, A&A, 514, A77
Kartaltepe, J. S., Sanders, D. B., Le Floc'h, E., et al. 2010, ApJ, 709, 572
Kennicutt, R. C. 1998, ARA&A, 36, 189
Kennicutt, R. C., Calzetti, D., Aniano, G., et al. 2011, PASP, 123, 1347
Kennicutt, R. C., Hao, C.-N., Calzetti, D., et al. 2009, ApJ, 703, 1672
Kroupa, P. 2002, Sci, 295, 82
Lagache, G., Dole, H., & Puget, J.-L. 2003, MNRAS, 338, 555
Lee, N., Le Floc'h, E., Sanders, D. B., et al. 2010, ApJ, 717, 175
Le Floc'h, E., Papovich, C., Dole, H., et al. 2005, ApJ, 632, 169
Lehmer, B. D., Brandt, W. N., Alexander, D. M., et al. 2005, ApJS, 161, 21
Lotz, J. M., Jonsson, P., Cox, T. J., et al. 2011, ApJ, 742, 103
Moorwood, A. F. M. 1986, A&A, 166, 4
Morrison, G. E., Owen, F. N., Dickinson, M., Ivison, R. J., & Ibar, E. 2010, ApJS, 188, 178
Moustakas, J., Kennicutt, R. C., Jr., Tremonti, C. A., et al. 2010, ApJS, 190, 233
Muxlow, T. W. B., Richards, A. M. S., Garrington, S. T., et al. 2005, MNRAS, 358, 1159
Muzzin, A., van Dokkum, P., Kriek, M., et al. 2010, ApJ, 725, 7
Narayanan, D., Cox, T. J., Hayward, C., & Hernquist, L. 2011, MNRAS, 412, 287
Noeske, K. G., Faber, S. M., Weiner, B. J., et al. 2007, ApJL, 660, L47
Nordon, R., Lutz, D., Genzel, R., et al. 2012, ApJ, 745, 182
Nordon, R., Lutz, D., Shao, L., et al. 2010, A&A, 518, L24
Papovich, C., Rudnick, G., Le Floc'h, E., et al. 2007, ApJ, 668, 45
Pérez-González, P. G., Rieke, G. H., Egami, E., et al. 2005, ApJ, 630, 82
Pope, A., Scott, D., Dickinson, M., et al. 2006, MNRAS, 370, 1185
Rex, M., Rawle, T. D., Egami, E., et al. 2010, A&A, 518, L13
Rieke, G. H., Alonso-Herrero, A., Weiner, B. J., et al. 2009, ApJ, 692, 556
Rigby, J. R., Marcillac, D., Egami, E., et al. 2008, ApJ, 675, 262
Rigopoulou, D., Spoon, H. W. W., Genzel, R., et al. 1999, AJ, 118, 2625
Roche, P. F., Aitken, D. K., Smith, C. H., & Ward, M. J. 1991, MNRAS, 248, 606
Roussel, H., Sauvage, M., Vigroux, L., & Bosma, A. 2001, A&A, 372, 427
Rovilos, E., Diamond, P. J., Lonsdale, C. J., Lonsdale, C. J., & Smith, H. E. 2003, MNRAS, 342, 373
Rujopakarn, W., Rieke, G. H., Eisenstein, D. J., & Juneau, S. 2011, ApJ, 726, 93
Rujopakarn, W., Rieke, G. H., Papovich, C. J., et al. 2012, ApJ, 755, 168
Salpeter, E. E. 1955, ApJ, 121, 161
Sanders, D. B., Mazzarella, J. M., Kim, D.-C., Surace, J. A., & Soifer, B. T. 2003, AJ, 126, 1607
Sanders, D. B., & Mirabel, I. F. 1996, ARA&A, 34, 749
Sanders, D. B., Salvato, M., Aussel, H., et al. 2007, ApJS, 172, 86
Siebenmorgen, R., & Krügel, E. 2007, A&A, 461, 445
Smith, J. D. T., Draine, B. T., Dale, D. A., et al. 2007, ApJ, 656, 770
Soifer, B. T., Sanders, D. B., Madore, B. F., et al. 1987, ApJ, 320, 238
Stetson, P. B. 1987, PASP, 99, 191
Symeonidis, M., Page, M. J., Seymour, N., et al. 2009, MNRAS, 397, 1728
Tacconi, L. J., Genzel, R., Neri, R., et al. 2010, Natur, 463, 781
Takagi, T., Ohyama, Y., Goto, T., et al. 2010, A&A, 514, A5
Thompson, T. A. 2009, in ASP Conf. Ser. 408, The Starburst-AGN Connection, ed. W. Wang, Z. Yang, Z. Luo, & Z. Chen (San Francisco, CA: ASP), 128
Thompson, T. A., Quataert, E., & Murray, N. 2005, ApJ, 630, 167
Tielens, A. G. G. M. 2008, ARA&A, 46, 289
Totani, T., Takeuchi, T. T., Nagashima, M., Kobayashi, M. A. R., & Makiya, R. 2011, PASJ, 63, 1181
Veilleux, S., Kim, D.-C., & Sanders, D. B. 2002, ApJS, 143, 315
Wilson, G. W., Hughes, D. H., Aretxaga, I., et al. 2008, MNRAS, 390, 1061
Wu, H., Cao, C., Hao, C.-N., et al. 2005, ApJL, 632, L79
Younger, J. D., Fazio, G. G., Wilner, D. J., et al. 2008, ApJ, 688, 59